rijksuniversiteit groningen

University of Groningen

Master thesis

Properties of Dwarf Galaxies in Fornax

Author:
M.J. Hutten

Supervisor:
Prof. dr. R. Peletier

January 22, 2017

Abstract

We investigate the properties of a sample of 28 dwarf galaxies taken from the Fornax Cluster Catalog (Ferguson, 1989) using data from the Fornax Deep Survey (FDS), obtained with the optical ESO VLT Survey Telescope (VST) in SDSS bands u', g', r' and i'. We use Galfit (Peng et al., 2010) for galaxy modeling and use aperture photometry to determine central magnitudes. We find that the luminosity-size relation and the magnitude-surface brightness relations are well approximated by an exponential and linear fit, with $\log(r_e) \propto -0.10\mathrm{M}_g$ and $\langle\mu_e\rangle_g \propto 0.48\mathrm{M}_g$. We find an average nucleation fraction of $\sim 39\%$ while $\sim 25\%$ are found nucleated in all four bands, in good agreement with similar studies. We cannot statistically reliably measure the color difference between the central parts of the galaxy and the galaxy as a whole. Finally, we reproduce a linear relation of Sérsic index (n) with luminosity as $n_g \propto -0.15\mathrm{m}_g$ which confirms the increase of n for brighter systems, and find evidence of a non-linear or non-continuous relation across larger magnitude ranges.

Contents

1 Introduction **2**

2 Sample and observations **4**
2.1 Data and reduction 4
2.2 Sample 5
2.3 Galaxy postage stamps 5

3 Methods **8**
3.1 Background-level determination 8
3.1.1 Sky-level determination: FCC123 9
3.2 Seeing correction 10
3.3 Aperture photometry: Magnitudes 12
3.3.1 Total magnitudes 12
3.3.2 Central magnitudes 13
3.4 Galaxy modeling: Galfit 13

4 Results **15**
4.1 Comparison between methods 15
4.1.1 Total magnitudes 15
4.1.2 Central magnitudes 15
4.2 Comparison with the FCC 18
4.3 Nucleation fraction and nucleus-to-galaxy luminosity ratio 19
4.4 Kormendy relations 21
4.5 Colours 22
4.5.1 Global colours 22
4.5.2 Central colours 23
4.5.3 Nucleus and global colours 24
4.6 Sérsic-index 25
4.6.1 Sérsic-index as a function of magnitude 26

5 Discussion **27**
5.1 Kormendy relations 27
5.2 Sérsic index 28
5.3 Central regions 29
5.4 Direct comparison with Muñoz et al. (2015) 29
5.5 Limitations of this study 31
5.6 Recommendations 32

6 Conclusions **34**

Appendices **36**

A Other tables **37**

Chapter 1

Introduction

Our Solar System is part of the (outskirts of) a spiral galaxy called the Milky Way. In this galaxy, there are many more Solar Systems, some similar to our own, some vastly different. In the same way, the Milky Way is surrounded similar and dissimilar galaxies in what is known as the Local Group, which in turn is part of the Virgo Supercluster. Our universe is built up from such a tree of clustering groups of objects, from sizes of individual stars up to galaxy clusters and filaments, that evolved from slightly overdense regions in the early universe to the rich variety of objects that we see today.

Galaxies in the early universe formed from the collapse of gas clouds. Hierarchical merging of many smaller galaxies into ever larger and larger ones which then started the formation of clusters through their gravitational attraction (Kauffmann and Haehnelt, 2000).

Cosmological simulations for the formation of structure in the universe predict that there are many more small, faint galaxies than their high luminosity counterparts (e.g. Moore et al., 1999; Springel et al., 2008), although we may not be able to observe most of them (also called the Missing Satellite Problem).

Dwarf galaxies are called such because they are smaller in radius, mass and total emitted light. They are observed to be much more dark matter dominated than their more luminous counterparts. Because of their low mass, they are much more sensitive to their environment. Physical mechanisms like ram-pressure stripping, galaxy harassment, tidal interactions, or mergers can heavily influence the galaxy morphology and star-formation rate. Because of this, large varieties in the morphology of dwarf galaxies are expected and indeed observed. Based on their appearance, dwarf galaxies can be classified into different categories, e.g. dwarf spheroidal (dSph), dwarf elliptical (dE), dwarf irregular (dIrr), dwarf S0 galaxies (dS0), blue cored dwarf (BCD), ultra compact dwarf (UCD), low surface brightness dwarf (LSB), but there is no clear physical evidence that the different categories really reflect different physical mechanisms and not just variations of the same object type. Most famous is the distinction between dSph and dE, first coined by Kormendy (1977), which is still subject of debate to this day.

Another question that still needs a definite answer is whether dwarf elliptical galaxies really are the low mass counterparts to giant ellipticals, as their name suggests. There are two major views in this debate. The first is that dwarfs are not the low luminosity counterparts of giant ellipticals, but an independent class of objects. This is concluded from studies of size, luminosity and surface brightness (SB); for dwarfs SB increases with galaxy luminosity, for giants elliptical galaxies this is the other way around (e.g. Graham and Guzmán, 2003). There is also a difference in the slope of the size-luminosity relation (Kormendy, 1977; Binggeli and Cameron, 1991; Bender et al., 1992; Kormendy et al., 2009). The second view is that the varying parameters are a natural consequence of a gradual variation in the galaxy light profile described by the Sérsic law (Sérsic, 1968), where $I(R) \propto \exp\left(R^{\frac{1}{n}}\right)$, with n the Sérsic index. The difference in SB-magnitude relations (and others) is the natural consequence of the linear relation between n and galaxy luminosity. Whether the relation between magnitude and n is really linear is however also still unclear.

What can be said is that from the morphology and colour, besides their sizes, dwarf- and giant ellipticals do look very much alike. But while ellipticals are often called to as 'red-and-dead', referring to their old red stellar populations, dwarf ellipticals are found to have a large variety in stellar populations, spanning an age range from around 1Gyr old to ages as comparable to the oldest objects in our universe (Michielsen et al., 2008; Koleva et al., 2009).

It is clear that there is still a lot to be discovered about dwarf galaxies. They are numerically dominant in our universe, but because of the technological challenges in observing them, it has been tricky to observe dwarf galaxies beyond the Local Group. However, because of continuous advances in telescope sensitivity it is becoming easier to probe dwarf galaxies, also outside of the local volume. This opens up new possibilities of studying faint galaxies in clusters like Virgo, Coma, or Fornax, which dramatically increases the total number of these objects that can be studied. One survey which aims to do so is the Fornax Deep Survey, a collaboration between the Kapteyn Astronomical Institute and the Instituto Nazionale Di Astrofisica (Astronomical Observatory of Capodimonte, Naples). It is from this survey that we have acquired our data.

Chapter 2 will be about this dataset and the sample we retrieve from it. In Chapter 3 we will explain our methods. Chapter 4 presents our results, which we discuss in Chapter 5. Finally, in Chapter 6 we summarize our findings and give our conclusions.

Chapter 2

Sample and observations

In this chapter we briefly summarize the origin of our data, its reduction, sample selection and the creation of galaxy stamps.

2.1 Data and reduction

Our data was obtained as the Fornax Deep Survey (FDS), performed with the ESO VLT Survey Telescope (VST) (Arnaboldi et al., 1998). The VST is located in Cerro Paranal, Chile and is a 2.6-meter optical survey telescope (Schipani et al., 2012). The 1° by 1° field of view instrument 'OmegaCAM' was used for imaging. OmegaCAM consists of an array of 8 by 4 ccd's of 2144 by 4200 pixels with an unbinned pixel size of 0.21". The total observation area of the cluster was divided in 1°x1° fields as shown in figure 2.1, which are all imaged in the OmegaCAM u', g', r' and i' SDSS bands (Kuijken et al., 2002; Kuijken, 2011). The total exposure times were 11000 s, 8000 s, 8000 s and 5000 s in u', g', r', and i', respectively. These were divided into individual exposures of 150 s. The central wavelength of the used bands are 3585Å, 4858Å, 6290Å, and 7706Å, for u', g', r' and i', respectively (Fukugita et al., 1995). Our analysis is based on one 1°x1° field from the FDS; field 16.

We briefly summarize the different data reduction steps in the instrumental corrections for our data, based on the work by Venhola et al. (2017, *in prep.*) *(in prep.)*. To reduce the OmegaCAM data, the AstroWISE environment (McFarland et al., 2013) was used to develop a pipeline. Dark current is defined from the overscan regions of the images and the row-wise median values are subtracted from the science images. Pixel-by-pixel variations in the dark noise are then removed by subtracting the overscan-corrected master bias image, which is created from a stack of eight bias images taken every night.

To counter small systematic flux variations across the instrument, an illumination correction is adopted from the Kilo-Degree Survey (KiDS, de Jong et al., 2015) and applied here. This illumination correction is generated by measuring point-source magnitudes across from flat-field corrected de-biased images. A second order polynomial plane is fitted to the error map and then multiplied with the science images.

The science-images are then flat-fielded by dividing the images by a master flat-field image, which is created by averaging 8 dome flat-fields and 8 twilight flat-fields, and then multiplying those average flat-fields with each other.

Having carried out the steps above, the images still have additional signal from atmospheric scattered light (background) that needs to be removed. Distinguishing between diffuse light from the sources and background light is not possible on low-luminosity-level single images, hence we make the assumption that the pattern of scattered light stays constant when the change in telescope pointing direction is small ($<$ a few degrees). The total sky level varies strongly depending on the time of observation, so all background images are scaled before they are combined. Background models for each CCD are then produced from a stack of 12 scaled images for each exposure (six

before and six after each exposure) and eventually subtracted from the final images.

OmegaCAM also has fringes (interference patterns) from internal reflections in the CCD's in the i'-band. These are corrected for in the background models, so no other fringe correction is needed.

Weight frames are generated by the pipeline for each exposure. These contain information on the noise level, bad pixels, cosmic rays, satellite tracks, and saturated pixels. For a detailed description of the weight frames and the creation of weight mosaics we refer to Venhola et al. (2017, *in prep.*). We adopt minimum magnitude errors taken from of 0.08 mag, 0.04 mag, 0.05 mag and 0.06 mag in u', g', r' and i', respectively (Venhola et al., 2017, *in prep*).

2.2 Sample

We select a number of sources from the Fornax Cluster Catalog (FCC) by Ferguson (1989) that are found in field 16 of the FDS. Field 16 is relatively close to the projected cluster center and can be seen as a probe for the entire cluster (see figure 2.1). The sources were selected by their total blue apparent magnitude (B_T) as reported in the FCC, and their morphological type. We set an upper limit to the total blue apparent magnitude of $B_T = 14.6$, which is the brightest Ferguson catalog galaxy that was given a morphological type including the name 'dwarf' or 'irregular'. We only select galaxies which are confirmed or likely members (member classification 1 or 2, respectively). Based on these conditions, we select 35 galaxies, as presented in table 2.2. Of these 35, 5 galaxies were excluded because of nearby or overlapping interfering sources, and a further two were excluded because of their morphology: FCC95 is a galaxy with clear spiral structure and a possible bar, and FCC115 is an edge on spiral galaxy. Both are unsuitable to be accurately fit by a simple Sérsic model. This gives us a total sample of 28 galaxies. The properties of the galaxy sample can be found in table 2.2.

2.3 Galaxy postage stamps

To ensure a subsequent quick and uniform data analysis, we create postage stamps of 1000 by 1000 pixels for every galaxy in our sample in all four bands, centered around the galaxy position as reported by Ferguson (1989). There is a small discrepancy in the positions provided by Ferguson (1989) and the visually perceived photo-center of our data in the order of 1". However, given that the pixel scale of our survey is 0.21 arcsec/pixel and the 1000 x 1000 pixel stamp size, this discrepancy does not need to be corrected for. The post stamps were created from the main field-files using Aladin (Bonnarel et al., 2000). Besides stamps for the sample galaxies we also create stamps from the weight frames corresponding to each galaxy, to be used when modeling using Galfit.

Table 2.1: Basic data for sample FCC galaxies

Name (1)	B_T (mag) (2)	Member (3)	Type (4)	Nuc. (5)	Selected (6)
FCC85	16.3	1	dE0,N	Y	1
FCC86	17.5	1	dE5,N?	P	1
FCC92	19.0	2	ImV or dE	N	2
FCC93	19.4	2	dE2	N	1
FCC94	19.3	1	dE0	N	1
FCC95	14.6	1	dSB0 or dSBa	N	3[a]
FCC97	19.0	1	dE1	N	1
FCC100	15.5	1	dE4,N	Y	1
FCC101	17.2	2	dE0,N or S	P	2
FCC103	19.3	1	dE2	N	1
FCC110	16.8	1	dE4	N	1
FCC114	19.7	2	dE1?	N	1
FCC115	16.6	2	Sdm(on edge)	N	3[b]
FCC116	16.1	1	dE1,N	Y	1
FCC123	16.7	1	ImV	N	1
FCC125	18.7	1	dE4	N	1
FCC127	19.8	2	dE3?	N	1
FCC130	18.2	2	ImV?	N	1
FCC131	20.3	2	dE3	N	1
FCC132	18.5	2	dE2	N	1
FCC133	17.5	1	dE0,N	Y	1
FCC136	14.8	1	dE2,N	Y	1
FCC137	16.9	1	dE0,N	Y	1
FCC140	19.0	1	dE4,N	Y	1
FCC142	18.5	1	dE2,N	Y	1
FCC144	19.2	1	dE0	N	1
FCC145	19.6	1	dE0	N	2
FCC146	19.5	2	dE4,N	Y	1
FCC154	19.2	1	dE3	N	2
FCC156	17.2	1	dE1	N	1
FCC157	18.3	1	dE0,N?	P	1
FCC158	16.8	1	dE6,N	Y	1
FCC160	17.7	1	dE1,N	Y	1
FCC163	19.8	1	dE0	N	2
FCC165	17.5	1	dE6	N	1

Notes. Column keys: (1) Galaxy name from the Fornax Cluster Catalog (Ferguson, 1989). (2) Blue apparent magnitude from FCC. (3) Membership status from FCC−1: confirmed member, 2: likely member. (4) Morphological type from FCC. (5) Nucleation from FCC− Y: Nucleated, N: Non-nucleated, P: Possibly nucleated (6) Selection in our sample−1: selected, 2: not selected on the basis of interfering nearby galaxy, 3: not selected based on morphology and subsequent issues regarding Sérsic fitting.

[a] Spiral galaxy with clear spiral structure and possible bar.

[b] Edge on spiral galaxy.

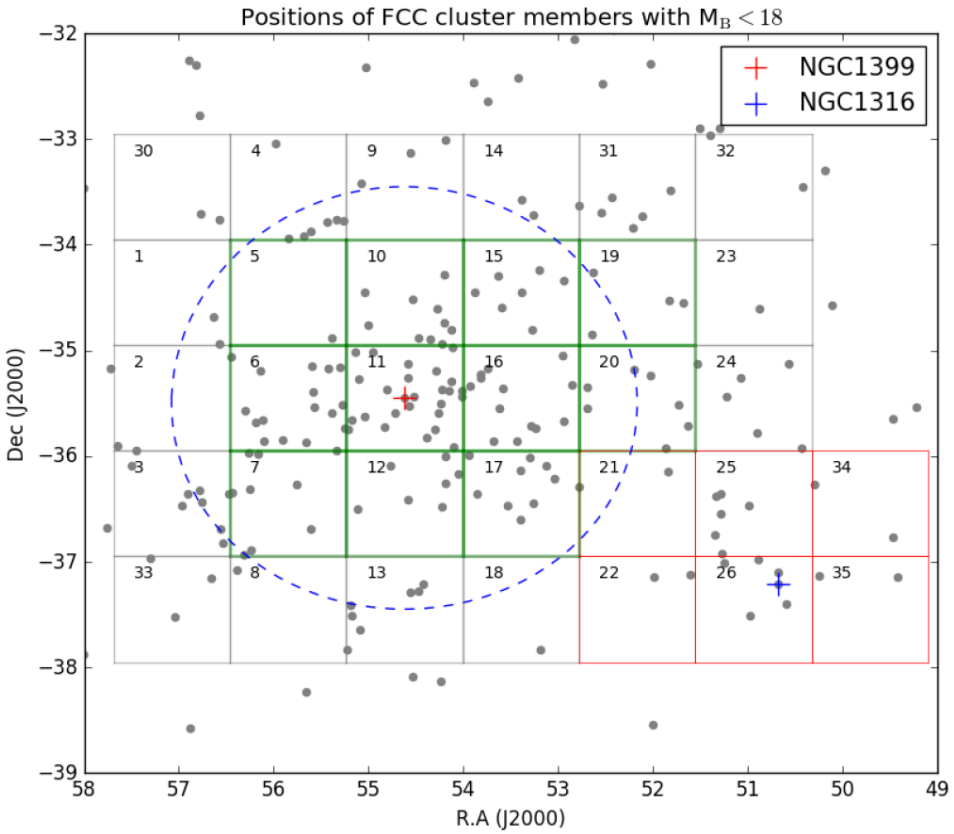

Figure 2.1: *Locations of the FDS fields plotted over the FCC galaxies (Ferguson, 1989) with* $B_T < -18$ *and member classification 1 or 2 (confirmed and likely member). Green bordered fields are ready in all filters by September 2016, and red bordered fields have only been partially imaged in r' and g'. Blue is the virial radius of Fornax (Drinkwater et al., 2001). Red and blue crosses highlight the cD galaxy NGC1399 in the core of Fornax and the elliptical shell galaxy NGC1316 which is the central galaxy of the Fornax-SW subcluster. Image and description taken from Venhola et al. (2017,* in prep.*)*

Chapter 3

Methods

In this chapter we will describe the methods used to analyze our sample of galaxies. We will be using two different techniques: aperture photometry and 2D-modeling. Aperture photometry as applied here is the addition of all flux within an aperture of a certain radius, of which the flux from the average background-levels and unwanted objects within the aperture has been subtracted. From this flux the magnitude within that aperture can be determined. For this we use the Graphical Astronomy and Image Analysis Tool (GAIA) (Currie et al., 2014). 2D-modeling is done using Galfit (Peng et al., 2010), which is a two-dimensional fitting algorithm that fits 2D analytic functions to galaxies and point sources.

We will be walking trough the steps in the order they were performed. We start from the determination of the background-level per image. Then we determine the FWHM for each band to be able to correct for seeing effects when measuring the brightness of nuclei, and perform aperture photometry. After this we model our sample galaxies using Galfit.

3.1 Background-level determination

The first major task for determining parameters for our galaxy sample is to accurately determine the background levels for every galaxy image. To do so, we perform aperture photometry using the program GAIA. We apply the following method of determining to the background-levels of an image.

We first multiply each pixel value with 10^{12} in order to not be limited by the detection threshold in GAIA. We then set the photometric zero-point in GAIA to 30, as

$$2.5 \log_{10} \left(10^{12}\right) = 30. \tag{3.1}$$

We determine a first estimate of the background value in circular apertures with a radius of 100 pixels. This is large enough to counter the influence of small objects caught in the aperture, but small enough to not have the apertures overlap. We then use the built in 'aperture photometry' tool to determine the modal pixel value within this aperture. Using the mean would result in a bias towards a higher background value due to the numerous small objects that are within the aperture.

We calculate the background value in 8 apertures, distributed along the image as seen in figure3.1. Whenever there is clear influence by a nearby bright star or source, the aperture is either shifted slightly (but never more than 100 pixels), or skipped. Assuming a constant background-level over the postage-stamp image, the final background is then the mean of the 8 measurements and its error is given by the standard deviation.

The initial estimates are then tested as follows. We fix the background in GAIA and measure the galaxy magnitude at (at least) three different radii. If the galaxy magnitude is constant independent of radius, we know that the estimate is accurate. If not, we increase or decrease the

background, depending on the outcome of the measurement, and try again until the results are consistent. The uncertainty in the backgrounds levels reflects how well they could be defined.

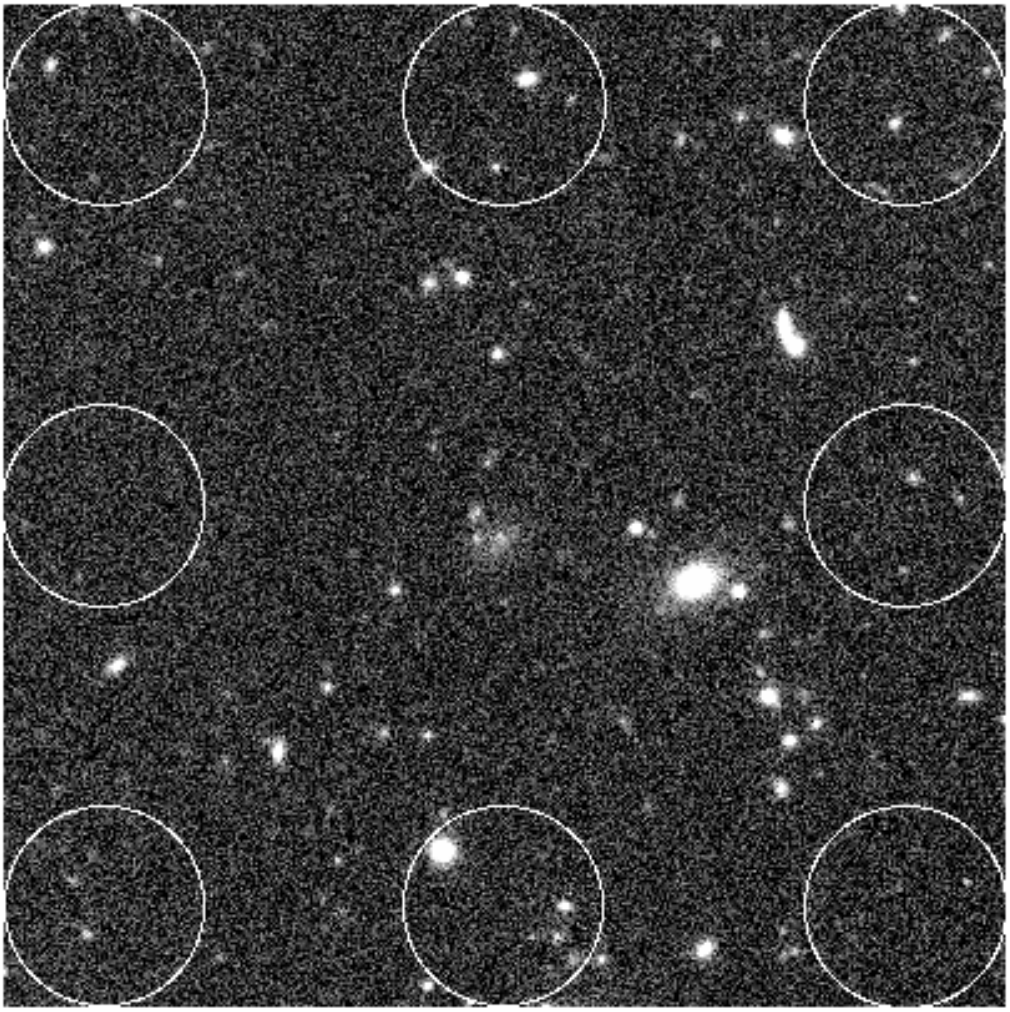

Figure 3.1: *Process of determining background-estimate using GAIA. The modal pixel value of the eight apertures is averaged and this serves as the starting estimate of the actual determination of the background. This postage-stamp's galaxy, FCC131, is seen in the center of the image.*

3.1.1 Sky-level determination: FCC123

We need to apply a slightly different method in the case of the galaxy FCC123, as there is a bright foreground star to its right. The star's stray light extends easily to the center of the galaxy, and therefore definitely influences the galaxy's background counts. This can also clearly be seen in figure 3.2.

Instead of assuming a constant background for this galaxy, we made an initial estimate of the background level by measuring at different points on the image that have the same projected radial distance from the star as the galaxy does. This way, the influence of the star is accounted for. The results from this method have been applied throughout this thesis for this specific galaxy.

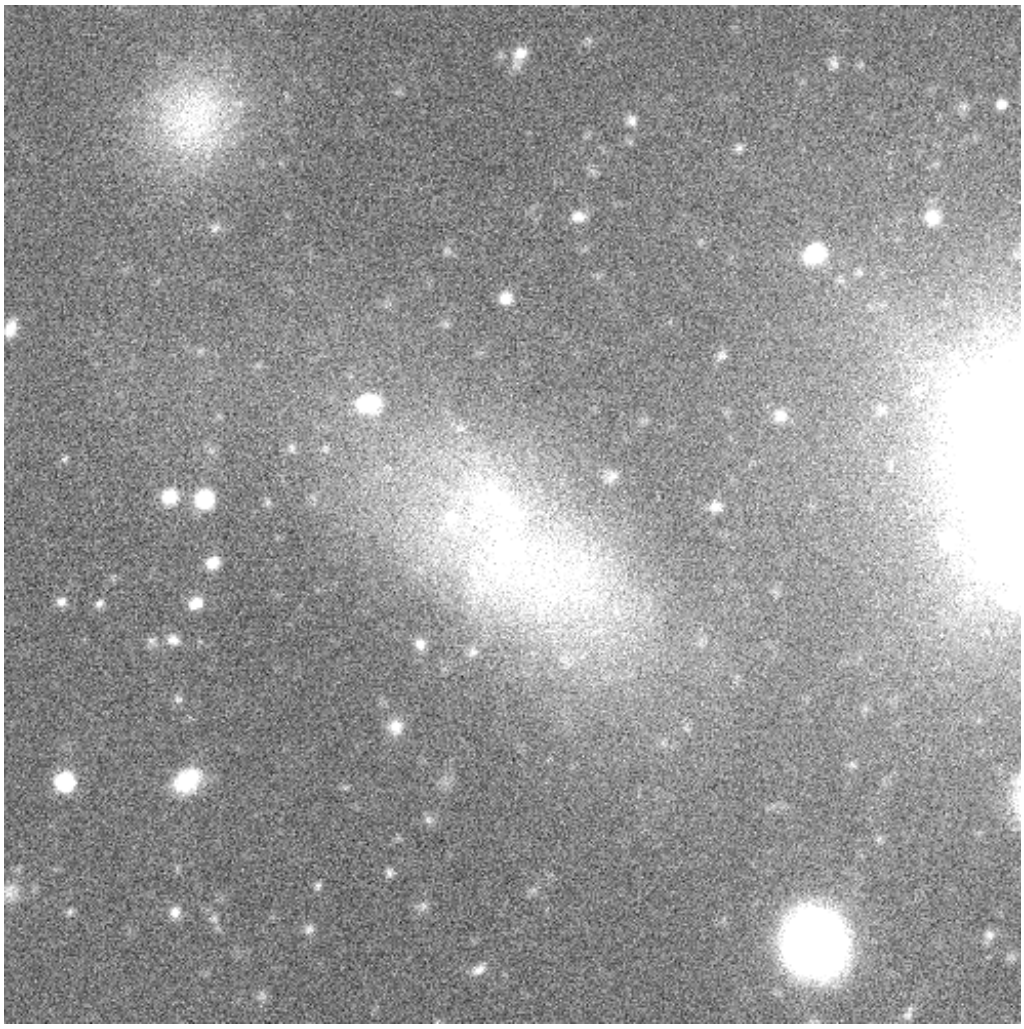

Figure 3.2: *g'-band image of galaxy FCC123 (center) with its nearby star to its right.*

3.2 Seeing correction

Seeing affects our data differently for all bands. To homogenize the photometry, we need to know the average FWHM of point-sources in all four bands. This will allow us to convert the data in all bands to the same spatial resolution, making it possible to determine accurate central colours. The determined FWHM will be used to convolve the data from the better resolution bands to the resolution of the band with the worst seeing.

We want to measure the FWHM of point-sources in all four bands. We assume that for each band the PSF is the same in each image. To determine the PSF we fit Gaussian profiles with Galfit to selected stars scattered throughout field 16. Stars were selected from two centrally located galaxy postage-stamps of field 16 (the images of galaxies FCC114 and FCC130), and from the outer regions (the images of galaxies FCC86 and FCC160). The selected stars were well isolated from contamination by nearby (in the line-of-sight) sources, and preferably among the faintest for that image, to avoid influence from saturation.

We assume a Gaussian PSF and determine the average FWHM for each band. One of the selected stars was deemed a probable binary star and excluded from the averages. Where possible we used the same star for all bands, but as most stars that are detectable in the u'-band are saturated in the other three bands, sometimes an alternative star was needed for the u'-band

image. Where this applies, we take a star that is located in the same galaxy image post-stamp. These stars are denoted by [a] in table 3.1.

Table 3.1: FWHM across photometric bands for selected stars.

#	Star-location image	FWHM (u')	FWHM (g')	FWHM (r')	FWHM (i')
1	FCC130	1.57"	1.50"	1.24"	1.41"
2[b]	FCC130	1.99"	1.82"	1.67"	1.82"
3	FCC114	1.62"[a]	1.51"	1.12"	1.28"
4	FCC86	1.40"	1.44"	1.12"	1.25"
5	FCC160	1.56"[a]	1.34"	1.33"	1.27"
6	FCC160	2.30"	1.48"	1.29"	1.31"
	Average	1.69"	1.46"	1.22"	1.30"

Notes.[a] Denotes that a different star from the same image has been used for the FWHM determination in the u-band. [b] Denotes a probable binary-star, which has been excluded from the average.

Having determined the average FWHM per band, we then convolve the r'- and i'-band images according to the retrieved FWHM. They are convolved to the lower resolution using the python module `convolve` from `astropy.convolution`. This module takes a the input image and a kernel to convolve with. The kernel is created automatically using the function `Gaussian2DKernel` (also from `astropy.convolution`), which takes only one argument, the σ of the Gaussian to convolve with. This is given as

$$\sigma_{c,r} = \sqrt{\left(\frac{\mathrm{FWHM}_g}{2.35}\right)^2 - \left(\frac{\mathrm{FWHM}_r}{2.35}\right)^2} = 0.341", \tag{3.2}$$

and likewise

$$\sigma_{c,i} = \sqrt{\left(\frac{\mathrm{FWHM}_g}{2.35}\right)^2 - \left(\frac{\mathrm{FWHM}_i}{2.35}\right)^2} = 0.283". \tag{3.3}$$

The resulting FWHM for the aforementioned stars are then recalculated, the results of which are found in table 3.2. While the correction is not perfect, the FWHM variation due to seeing effects has been significantly reduced. Because of the lower resolution of the u'-band images, as evidenced by the average FWHM presented in table 3.1, these were not used in the remainder of this study. Therefore, there was no need to convolve the other bands to the u'-band resolution.

Table 3.2: FWHM across photometric bands for selected stars after seeing correction.

#	Star-location image	FWHM (g')	FWHM (r')	FWHM (i')
1	FCC130	1.50"	1.51"	1.53"
3	FCC114	1.51"	1.37"	1.44"
4	FCC86	1.44"	1.43"	1.37"
5	FCC160	1.34"	1.55"	1.39"
6	FCC160	1.48"	1.59"	1.44"
	Average	1.46"	1.49"	1.43"

3.3 Aperture photometry: Magnitudes

Now that we have determined the background levels per image, and know the FWHM for each band, we can start to determine the magnitudes of our sample galaxies. We will determine both global magnitudes, and central magnitudes. The process is visualized in figure 3.3.

3.3.1 Total magnitudes

An appropriate aperture radius is chosen such that all light from the galaxy is inside the aperture. Unfortunately, as the current version of GAIA only supports circular apertures, the magnitudes stated in this section are calculated therein, even if that does not reflect the morphology. We also have to determine the magnitude of interfering sources to be able to subtract them. The threshold for a source to be subtracted is when at least half the source is within the aperture used for the galaxy, and the interfering source's total magnitude is not more than 6 magnitudes fainter than the galaxy. This is equivalent to at most $\sim 0.4\%$ contribution from a non-subtracted source. The light from the interfering sources is then subtracted from the light from the galaxy as follows. All magnitudes are converted into flux by

$$f = 10^{0.4(30-m)}. \tag{3.4}$$

This is done for all sources. The flux originating from all sources except the main galaxy is then subtracted from the total flux. The corrected total magnitude then becomes

$$m = 30 - 2.5 \log_{10} \left(f_{gal} - f_{sources,tot} \right). \tag{3.5}$$

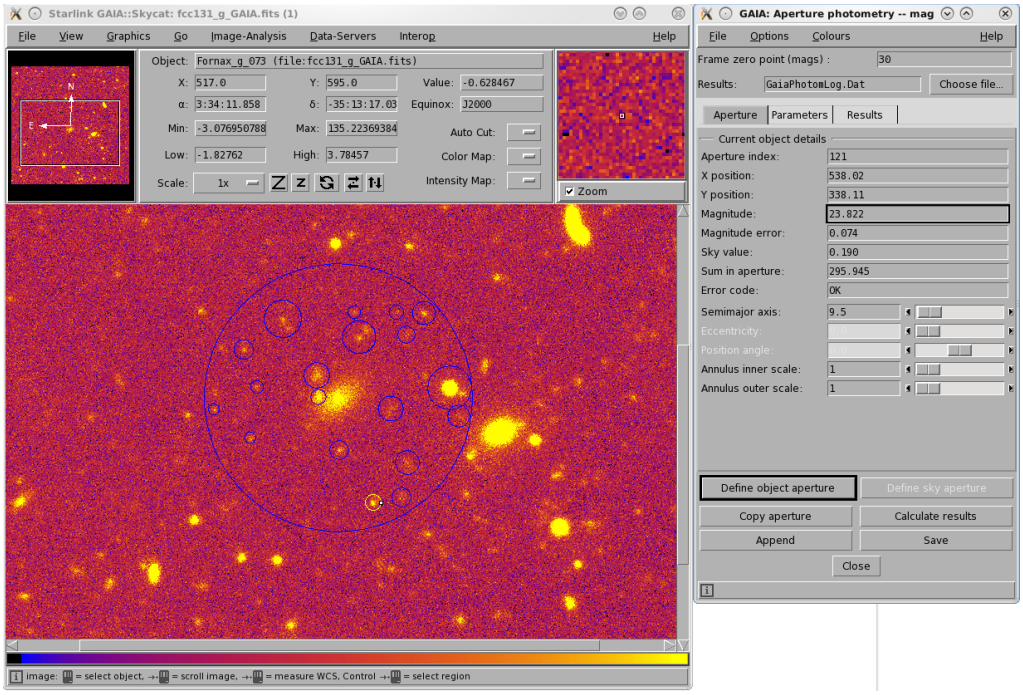

Figure 3.3: *Aperture photometry method using GAIA. Left: the galaxy image, the galaxy's aperture and the fore- and background source apertures whose flux will be subtracted from the total flux. Right: GAIA aperture photometry module with parameters.*

Naturally, the flux from nuclei for nucleated galaxies was not subtracted. In the next section we show how we determine the central magnitudes for all galaxies.

3.3.2 Central magnitudes

We assume the nuclei of our galaxies have typical sizes that do not exceed 100 parsec (Turner et al., 2012), which at a distance modulus of 31.51, or alternatively a distance of 20.0 Mpc (Blakeslee et al., 2009) corresponds to ∼1.03". This means that our nuclei are unresolved. Even smaller radii are found by den Brok et al. (2014), with ∼70% of their nuclei radii being ≤ 9 pc in Coma. This is less than our determined FWHM for all bands, thus we can treat the nuclei of our galaxy as point-sources in our measurements.

Having convolved all bands to similar resolution we use the same aperture radius in all bands. We take an aperture radius of 2 seeing σ's, to maximize the amount of central light whilst minimizing the influence from the underlying galaxy. This corresponds to an aperture radius of 1.24" or 6 pixels (rounded up to the nearest full pixel value).

3.4 Galaxy modeling: Galfit

While aperture-photometry is useful for determining total apparent magnitudes, it cannot be used to derive other parameters such as ellipticity, Sérsic index, and radius. Therefore, we use the 2D-modeling tool 'Galfit' by Peng et al. (2010). This allows us to fit analytic functions to our galaxy images. From provided initial guesses and selected galaxy components, it runs a χ^2 reduction routine that, given reasonable initial estimates, returns the best-fit model for that image. In this study we fit a single Sérsic model (Sérsic, 1968) to our galaxies, and add a central Gaussian component where necessary. The necessity of adding a Gaussian component to the Galfit model to achieve accurate results or even just convergence, determines whether a galaxy is classified as nucleated or non-nucleated in this study.

The Sérsic profile is a three parameter model with the form

$$I(r) = I_e \exp\left(-b_n\left[\left(\frac{r}{r_e}\right)^{1/n} - 1\right]\right). \tag{3.6}$$

Here I_e is the intensity at the effective radius, r_e. The Sérsic index n characterizes the overall shape of the light profile, and b_n is a function of the Sérsic index. Any fore- or background sources that could influence the result or convergence of Galfit were masked before running it.

Though Galfit is quite robust, convergence depends heavily on the initial input. Therefore, as many initial parameters as possible were taken from Ferguson (1989) to give a best chance of convergence on the first try. These parameters are apparent magnitude (m) (B_T magnitude with colour corrections for the different bands) and effective radius (r_e). Galfit returns not only best-fit parameters, but also images of the best-fit model and a residual image where the best-fit model is subtracted from the original image. An example of this is found in figure 3.4.

For every image we run three separate Galfit models, one for the best guess for the background-levels and one for both the minimal and maximal levels. These guesses are kept fixed during the fitting procedure. The differences in retrieved parameters from these models will provide us with reasonable margins on our results, which in the remainder of this thesis we will use as error estimates.

Galfit is used to obtain the following parameters with which we perform our analysis: m, $r_e$and n. From these parameters, the mean effective surface brightness (the mean surface brightness enclosed within r_e), can be obtained via

$$\langle\mu\rangle_e = \mathrm{m} + 2.5\log_{10}\left(2\pi {r_e}^2\right). \tag{3.7}$$

A detailed derivation can be found in Graham and Driver (2005). In the remainder of the thesis we will refer to 'surface brightness' as defined in the equation above.

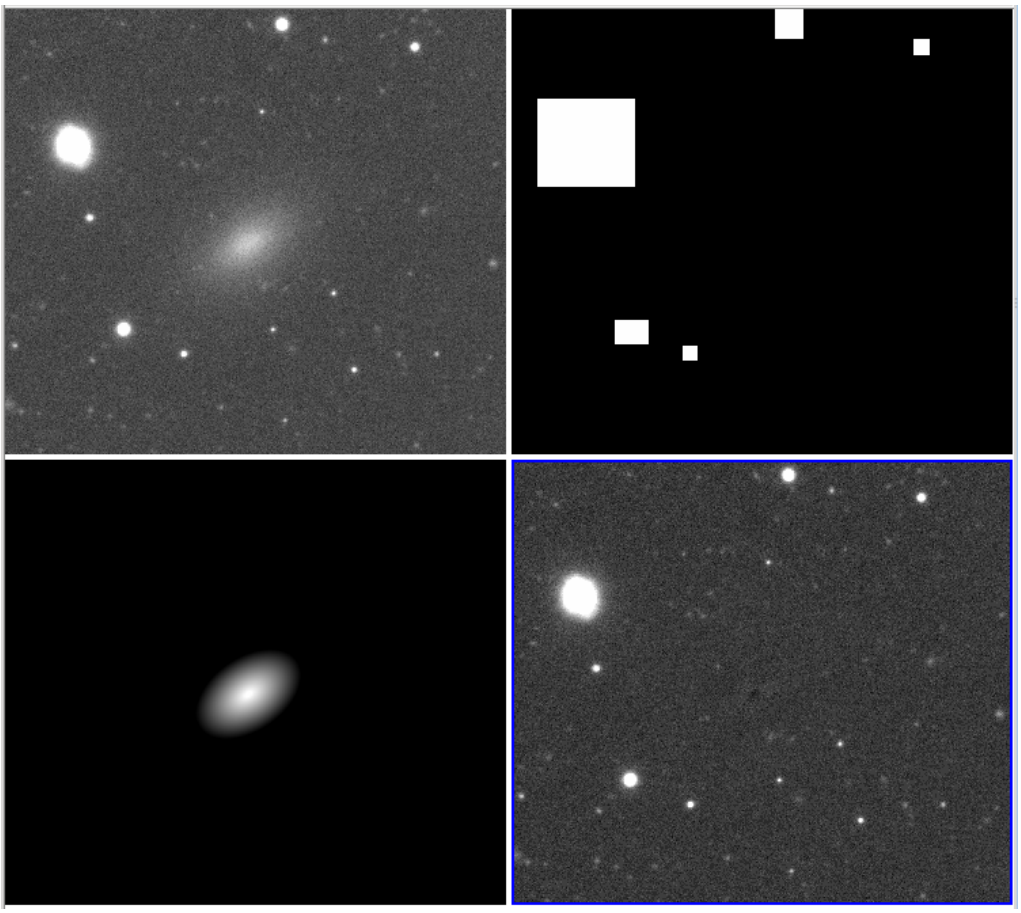

Figure 3.4: *Top left: Galaxy stamp for g'-band image of FCC110. Top right: Pixel mask. Bottom left: Galfit galaxy model. Bottom right: Residual after subtraction of model from original image.*

Chapter 4

Results

In this section we will take a closer look at the derived parameters of the sample galaxies, and their nuclei. We will mainly be using the g'- and r'-band results, and where desirable refer to i'-band results. The results from the g-band models are shown in table 4.1 (and results from other bands are found in the appendix). All stated parameters are derived from galaxy modeling with Galfit, apart from the central magnitudes, which have been derived using GAIA, as detailed in the previous chapter.

4.1 Comparison between methods

We briefly compare the results of the two different methods used in this study (2D modeling with Galfit and aperture photometry with GAIA) and reflect on their merits. A slight offset between the central magnitudes originating from the different measuring techniques is to be expected.

4.1.1 Total magnitudes

Figure 4.1 shows a comparison of the measured or modeled g'-band magnitudes from aperture photometry using GAIA and galaxy modeling using Galfit. It is clear that magnitudes derived by Galfit are on average brighter than their counterparts calculated with GAIA. Because both methods use the same background estimations, this cannot be the source of the discrepancy. One might even expect that as the aperture radius increases, aperture photometry inevitably acquires more light within that radius because not every nearby source could be eliminated, though the remaining sources are very small and faint. However, it may be that the faint tail of the light-curve of the galaxy fell outside the used apertures, even though we specifically attempted at avoiding this, regularly using radii beyond which the galaxy was visible. The determined g-band magnitude of FCC123 with GAIA could not be optimized because of a nearby interference (see section 3.1.1), hence the large discrepancy between the Galfit and GAIA result for this galaxy. Based on our findings and the flexibility of Galfit, we will be using those results for the remainder of this thesis.

4.1.2 Central magnitudes

We expect the greatest difference between the two methods to be the difference in central magnitudes. The offsets are plotted in figure 4.2. These differences stem from a number of factors, described below.

Firstly, when performing aperture photometry it is not possible to eliminate the underlying galaxy from the central part, without prior knowledge of its size, brightness and shape of the galaxy. These are unknown, unless we use parameters originating from Galfit, but this would compromise the independence of the measurements. Therefore, we do not subtract light from the galaxy in the central aperture and thus all central magnitudes with measured by aperture photometry will have residual light from their host. We expect however that at the chosen small radii, the total light

Table 4.1: *Results for sample galaxies in the g'-band and galactic (g'-r') colour. Tables with the remaining data from the other bands are found in Appendix A.*

Name	g' (mag)	$r_{e,g}$ (")	$\langle\mu\rangle_e$ (mag/"^{2})	n_g	(g'-r') (mag)	nucl.	g'$_n$ (mag)
(1)	(2)	(3)	(4)	(5)	(6)	(7)	(8)
FCC85	$15.93^{+0.04}_{-0.04}$	$16.7^{+0.4}_{-0.4}$	$24.03^{+0.04}_{-0.04}$	$1.49^{+0.04}_{-0.03}$	$0.67^{+0.03}_{-0.03}$	Y	$20.23^{+0.04}_{-0.04}$
FCC86	$17.19^{+0.10}_{-0.08}$	$18.0^{+1.7}_{-1.1}$	$25.46^{+0.10}_{-0.07}$	$1.21^{+0.10}_{-0.07}$	$0.88^{+0.49}_{-0.23}$	N	$22.01^{+0.04}_{-0.04}$
FCC93	$19.59^{+0.15}_{-0.13}$	$9.3^{+1.4}_{-1.0}$	$26.42^{+0.15}_{-0.13}$	$1.20^{+0.14}_{-0.14}$	$0.59^{+0.19}_{-0.16}$	N	$23.24^{+0.04}_{-0.04}$
FCC94	$19.47^{+0.11}_{-0.09}$	$7.8^{+0.5}_{-0.4}$	$25.93^{+0.04}_{-0.04}$	$0.62^{+0.06}_{-0.04}$	$0.76^{+0.12}_{-0.10}$	N	$23.47^{+0.04}_{-0.04}$
FCC97	$19.15^{+0.13}_{-0.04}$	$10.3^{+0.0}_{-0.0}$	$26.21^{+0.04}_{-0.04}$	$0.62^{+0.04}_{-0.04}$	$0.65^{+0.22}_{-0.27}$	N	$23.64^{+0.04}_{-0.04}$
FCC100	$15.30^{+0.04}_{-0.04}$	$20.5^{+0.5}_{-0.4}$	$23.86^{+0.04}_{-0.04}$	$1.32^{+0.03}_{-0.02}$	$0.66^{+0.03}_{-0.03}$	N	$20.19^{+0.04}_{-0.04}$
FCC103	$19.34^{+0.04}_{-0.04}$	$9.6^{+0.2}_{-0.2}$	$26.24^{+0.04}_{-0.04}$	$0.83^{+0.02}_{-0.02}$	$0.69^{+0.10}_{-0.07}$	N	$23.11^{+0.04}_{-0.04}$
FCC110	$16.90^{+0.04}_{-0.04}$	$18.6^{+0.3}_{-0.3}$	$25.24^{+0.04}_{-0.04}$	$0.99^{+0.02}_{-0.02}$	$0.74^{+0.06}_{-0.05}$	N	$22.09^{+0.04}_{-0.04}$
FCC114	$20.00^{+0.04}_{-0.04}$	$7.3^{+0.2}_{-0.2}$	$26.33^{+0.04}_{-0.04}$	$0.75^{+0.03}_{-0.03}$	$0.56^{+0.04}_{-0.04}$	N	$23.43^{+0.04}_{-0.04}$
FCC116	$15.82^{+0.04}_{-0.04}$	$16.5^{+0.6}_{-0.6}$	$23.90^{+0.04}_{-0.04}$	$1.38^{+0.04}_{-0.04}$	$0.70^{+0.05}_{-0.05}$	N	$20.55^{+0.04}_{-0.04}$
FCC123	$16.84^{+0.14}_{-0.12}$	$29.3^{+2.6}_{-1.9}$	$26.17^{+0.04}_{-0.04}$	$0.60^{+0.07}_{-0.05}$	$0.74^{+0.23}_{-0.20}$	N	$22.32^{+0.04}_{-0.04}$
FCC125	$18.71^{+0.09}_{-0.07}$	$10.4^{+0.7}_{-0.5}$	$25.79^{+0.06}_{-0.04}$	$0.73^{+0.07}_{-0.05}$	$0.90^{+1.49}_{-0.18}$	N	$23.30^{+0.04}_{-0.04}$
FCC127	$19.40^{+0.09}_{-0.07}$	$8.4^{+0.7}_{-0.5}$	$26.02^{+0.08}_{-0.06}$	$0.99^{+0.08}_{-0.06}$	$0.60^{+0.14}_{-0.11}$	N	$23.24^{+0.04}_{-0.04}$
FCC130	$18.25^{+0.28}_{-0.14}$	$19.4^{+4.9}_{-1.6}$	$26.69^{+0.21}_{-0.05}$	$0.73^{+0.29}_{-0.09}$	$1.03^{+0.64}_{-0.31}$	N	$24.50^{+0.04}_{-0.04}$
FCC131	$20.12^{+0.04}_{-0.04}$	$6.4^{+0.2}_{-0.2}$	$26.13^{+0.04}_{-0.04}$	$0.90^{+0.05}_{-0.04}$	$0.44^{+0.06}_{-0.05}$	N	$23.15^{+0.04}_{-0.04}$
FCC132	$18.21^{+0.04}_{-0.04}$	$6.5^{+0.1}_{-0.1}$	$24.27^{+0.04}_{-0.04}$	$0.87^{+0.01}_{-0.01}$	$0.77^{+0.02}_{-0.02}$	N	$21.48^{+0.04}_{-0.04}$
FCC133	$16.92^{+0.66}_{-0.36}$	$22.4^{+26.3}_{-7.2}$	$25.67^{+1.03}_{-0.48}$	$1.83^{+1.05}_{-0.56}$	$-^a$	Y	$21.33^{+0.04}_{-0.04}$
FCC136	$14.56^{+0.06}_{-0.05}$	$18.6^{+1.4}_{-1.0}$	$22.91^{+0.09}_{-0.07}$	$1.80^{+0.10}_{-0.08}$	$0.86^{+0.10}_{-0.09}$	Y	$18.96^{+0.04}_{-0.04}$
FCC137	$16.74^{+0.05}_{-0.05}$	$15.4^{+0.7}_{-0.7}$	$24.68^{+0.05}_{-0.05}$	$1.19^{+0.06}_{-0.06}$	$0.69^{+0.21}_{-0.14}$	Y	$21.25^{+0.04}_{-0.04}$
FCC140	$18.64^{+0.16}_{-0.13}$	$10.8^{+1.6}_{-1.1}$	$25.81^{+0.14}_{-0.09}$	$0.92^{+0.14}_{-0.14}$	$0.74^{+0.19}_{-0.16}$	Y	$22.22^{+0.04}_{-0.04}$
FCC142	$18.46^{+0.14}_{-0.12}$	$11.5^{+1.4}_{-1.0}$	$25.75^{+0.11}_{-0.07}$	$1.00^{+0.00}_{-0.00}$	$0.47^{+0.17}_{-0.14}$	Y	$21.99^{+0.04}_{-0.04}$
FCC144	$19.45^{+0.04}_{-0.04}$	$6.5^{+0.1}_{-0.1}$	$25.50^{+0.04}_{-0.04}$	$0.73^{+0.02}_{-0.02}$	$0.82^{+0.03}_{-0.03}$	N	$22.74^{+0.04}_{-0.04}$
FCC146	$19.54^{+0.05}_{-0.04}$	$6.3^{+0.2}_{-0.2}$	$25.52^{+0.04}_{-0.04}$	$0.88^{+0.04}_{-0.03}$	$0.65^{+0.05}_{-0.05}$	N	$22.42^{+0.04}_{-0.04}$
FCC156	$17.07^{+0.04}_{-0.04}$	$16.1^{+0.3}_{-0.2}$	$25.11^{+0.04}_{-0.04}$	$1.03^{+0.02}_{-0.02}$	$0.69^{+0.06}_{-0.05}$	N	$22.02^{+0.04}_{-0.04}$
FCC157	$18.13^{+0.07}_{-0.04}$	$16.3^{+1.0}_{-1.0}$	$26.18^{+0.05}_{-0.04}$	$0.85^{+0.00}_{-0.00}$	$0.88^{+0.20}_{-0.13}$	Y	$22.73^{+0.04}_{-0.04}$
FCC158	$16.66^{+0.24}_{-0.11}$	$22.0^{+5.8}_{-2.0}$	$25.37^{+0.27}_{-0.09}$	$1.08^{+0.33}_{-0.13}$	$0.66^{+0.69}_{-0.27}$	Y	$21.01^{+0.04}_{-0.04}$
FCC160	$17.37^{+0.27}_{-0.05}$	$14.2^{+3.5}_{-0.0}$	$25.13^{+0.21}_{-0.04}$	$1.08^{+0.17}_{-0.17}$	$1.15^{+0.44}_{-0.13}$	Y	$21.88^{+0.04}_{-0.04}$
FCC165	$17.47^{+0.04}_{-0.04}$	$14.7^{+0.3}_{-0.3}$	$25.30^{+0.04}_{-0.04}$	$0.81^{+0.02}_{-0.02}$	$0.71^{+0.13}_{-0.10}$	Y	$21.92^{+0.04}_{-0.04}$

Notes. Column keys: (1) Galaxy name from the Fornax Cluster Catalog (Ferguson, 1989). (2) g-band magnitude as determined by Galfit (in magnitudes). (3) Effective radius in arcsec from Galfit-fitting. (4) Calculated effective mean surface brightness (in magnitudes per square arcsec). (5) Sérsic index. (6) Galaxy (g'-r') colour (in magnitudes). (7) Nucleated fit (Y) or non-nucleated (N) fit. (8) g'-band central magnitude.

[a] FCC133 has no fit in the r'-band

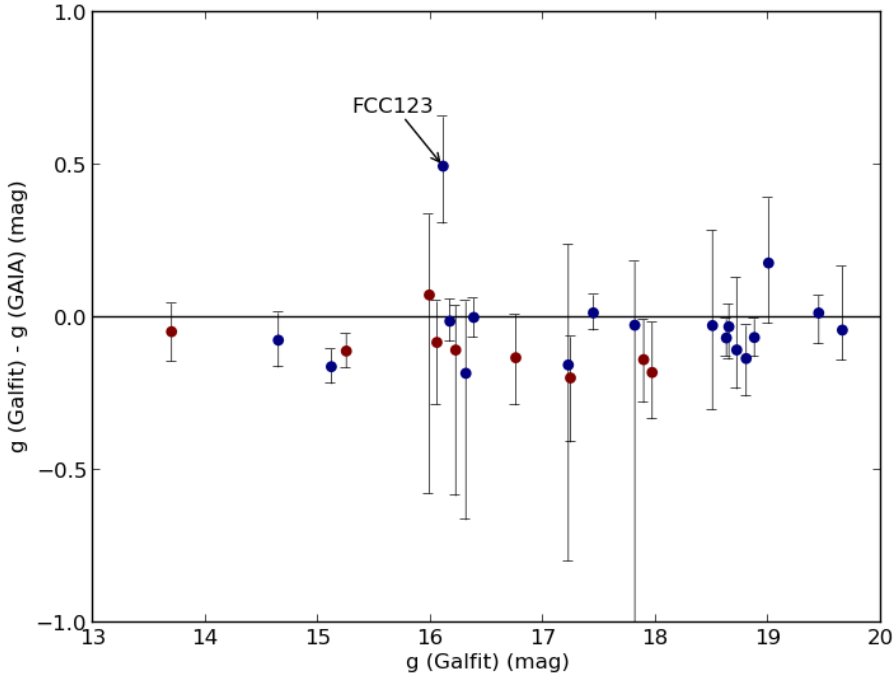

Figure 4.1: *Comparison of magnitudes retrieved by GAIA and Galfit. Red circles are nucleated galaxies, blue are non-nucleated.*

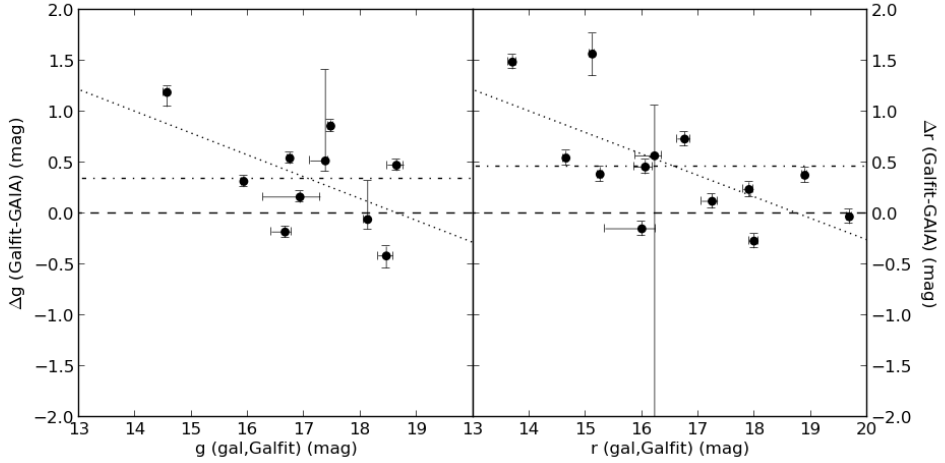

Figure 4.2: *Comparison between central magnitudes as a function of their Galfit-derived total galaxy magnitude.* Δg *and* Δr *are given by* g_{nuc}*(Galfit)-*g_{nuc}*(GAIA) and* r_{nuc}*(Galfit)-*r_{nuc}*(GAIA) in the left and right image, respectively. The dashed line denotes* $\Delta = 0$*, the dashed-dotted line is the average offset per band, and the dotted line is the best linear fit for the offset in magnitudes. Only galaxies marked as nucleated in the respective bands are shown.*

within the aperture is dominated by the light from the nucleus. While Galfit includes the light from the tails of the Gaussian to calculate the total magnitude, aperture photometry with GAIA

has a discrete cut off outside of the aperture. Also, Galfit fits ellipses (although mostly with an axis ratio of ~ 1) whereas all the GAIA apertures are circular (see section 3.3.1).

The average offset between nucleus magnitudes in g' and r' are 0.34 mag and 0.46, respectively. It is clear that brighter galaxies have a larger effect on the central magnitude than smaller galaxies, as their nuclei are fainter with respect to the Sérsic component, as detailed in the following section. Therefore we determine a linear fit to the offset, denoted by the dotted line in figure 4.2. The best-fit slopes and offsets are the same in both the g'- and the r'-band, with $\Delta = -0.21 m_{g/r} + 4.0$. This leads us to believe that there is a systematic discrepancy between GAIA and Galfit nucleus magnitudes.

In choosing which parameter to use when diagnosing the central regions of the galaxies, we decided to use the GAIA determined magnitudes. Even though the addition of the central Gaussian in Galfit modeling was indispensable for acquiring a correct model for the nucleated galaxies, the aperture photometry is the better known and tested method. In this case it is also the most flexible, because it can provide us with information on the centers of non-nucleated galaxies. Therefore, we will be using the aperture photometry derived central magnitudes throughout this study, unless mentioned otherwise.

4.2 Comparison with the FCC

To evaluate the results obtained in our sample, we compare it with the most relevant studies from literature.

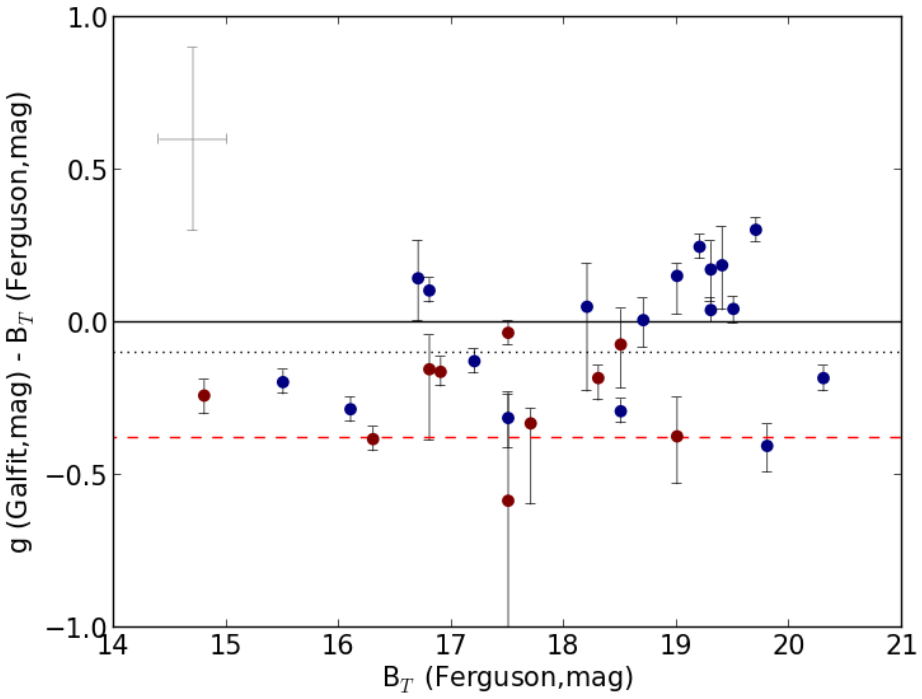

Figure 4.3: *Galfit g'-band results compared to B_T magnitude reported by Ferguson (1989). Nucleated galaxies are plotted in red, non-nucleated in blue. The red dashed line is the expected offset of -0.38 (Fukugita et al., 1995), the black dotted line our average offset of -0.10. Standard errors from Ferguson (1989) in the top left, plotted errors are from our sample alone.*

We first compare our results to the FCC Ferguson (1989). As Ferguson (1989) measured

magnitudes in the B-band, we need to take the filter transformation of (g'$-B_T$) = -0.38 (Fukugita et al., 1995) into account. The results of the comparison are shown in figure 4.3, where the red dashed line at (g-B_T) = -0.38 represents the expected value.

Not all galaxies match to our expectation for the offset. Though for most galaxies the offset is within the errors, there is is a clear tendency of our galaxies being fainter than reported by Ferguson (1989) when taking into account the colour transformation. This could partly be because the aforementioned transformation is dependent on galaxy type, and although our sample of dwarf ellipticals is expected to have colours very similar to the giant ellipticals mentioned in Fukugita et al. (1995), the comparison is not ideal.

The average offset between the g'-band magnitude and B-band magnitude is -0.1 mag and shown with a dotted line in figure 4.3. Ferguson (1989) reports rather large errors ($\pm$0.3mag). It must be noted that these galaxies that we are now studying were just barely above the detection limit at the time Ferguson published his work.

4.3 Nucleation fraction and nucleus-to-galaxy luminosity ratio

In this section we will show the nucleation fraction compared to Ferguson (1989), calculate the nucleus-to-galaxy luminosity ratio for all our nucleated galaxies and report on the found trend between galaxy magnitude and relative brightness of the nucleus.

Out of our final sample of 28 galaxies, 10 were found to be nucleated in the g'-band, which is a percentage of $\sim$36%. For u', r', and i', the corresponding nucleation fractions are 8/28 ($\sim$29%), 13/27 ($\sim$48%), and 12/28 ($\sim$43%), respectively. In total 14 out of 28 galaxies show nucleation in one band or more ($\sim$50%), whereas 7 show nucleation in all bands ($\sim$25%). We can compare the magnitude of the nuclei with the magnitude of their hosts, which we do here, or compare the nucleus' colours (eg. (g'-r'), (g'-i'), etc.) with their hosts, as in section 4.5.2. We confirm the nucleation of all 11 galaxies that were classified as such by Ferguson (1989) in at least one band or more (see table 2.2). Of the two possibly nucleated galaxies, FCC86 and FCC157, we do not confirm the first to be nucleated, but do confirm the latter. Besides this, we find evidence of nucleation in two more galaxies: FCC131 in the r'-band, and FCC165 in the g', r' and i' band. Studies by Lotz et al. (2004) and Turner et al. (2012) also report additional nuclei in galaxies that were not classified as nucleated by Ferguson (1989).

Figure 4.4 shows the nucleus and galaxy magnitudes and the nucleus-to-galaxy light ratio in the g- and r'-band, respectively. It is clear, especially from the lower panels, that in brighter galaxies a smaller percentage of light originates from the nucleus of the galaxy. Here we use the Galfit central parameters, to be able to distinguish light from the nucleus from the main body of the galaxy. Lower nucleus-to-galaxy light ratios for brighter galaxies could lead to the notion that all galaxy nuclei have similar luminosity regardless their host, but the top half of figure 4.4 shows that the brightness of nuclei do scale with the host galaxy magnitude. For all g'-band nuclei we find a slope of

$$g_{nuc} \propto 0.61 g_{gal} \tag{4.1}$$

and for r' this is

$$r_{nuc} \propto 0.44 r_{gal}. \tag{4.2}$$

When combining the results, our retrieved total average slope becomes $m_{nuc} \propto 0.49 m_{gal}$. When we only take into account galaxies that are nucleated in both g' and r' (9 in total), this eliminates some of the effects of outliers. Doing so, we get that $g_{nuc} \propto 0.61 g_{gal}$ (black dashed line in top left image of figure 4.4) and $r_{nuc} \propto 0.54 r_{gal}$ (black dashed line in top right image of figure 4.4) with an average slope of $m_{nuc} \propto 0.56 m_{gal}$ (black solid line in top images of figure 4.4, both left and right), so the few galaxies that are only (visibly) nucleated in r' have quite a big influence on the slope.

We find that the slope coincides very well with the results of den Brok et al. (2014) who report that $M_{nuc} \propto 0.57 M_{gal}$ in the F814W-band (red dashed line in top images of figure 4.4). The offset between our sample and that of den Brok et al. (2014) can be explained by the fact that their data

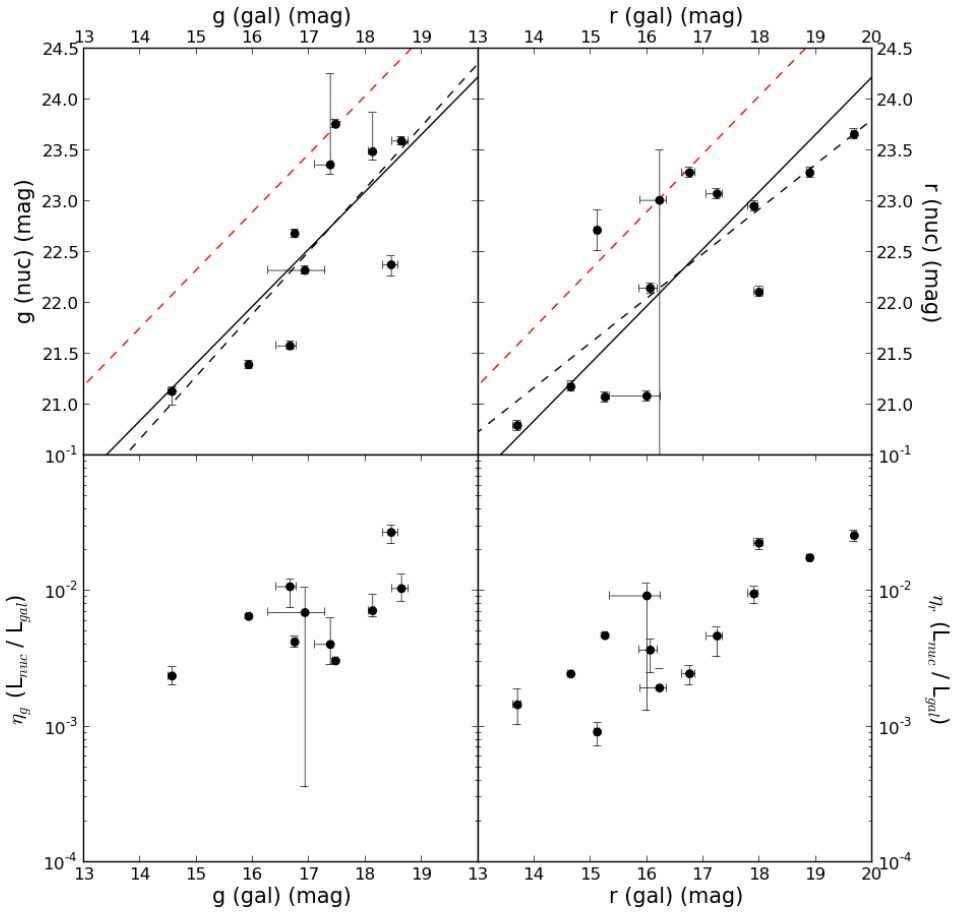

Figure 4.4: *Top: Galaxy and nucleus appearant magnitudes in the g'-band (left) and r'-band (right). Black dashed line is the best fit for the respective band, black solid line is the best fit across both bands (taking into account only galaxies that have nuclei in both bands), and the red dashed line is the best fit from den Brok et al. (2014) (with HST). Bottom: Nucleus-to-galaxy light ratio in the g'-band (left) and r'-band (right).*

was obtained with HST, which has a much better resolution than the FDS, which leaves our nuclei still unresolved. Additionally, their method of obtaining the central magnitude was different from ours.

Turner et al. (2012) also note that fainter galaxies on average show brighter nuclei when compared to their host magnitude, though their sample shows quite a bit of scatter compared to our set and shows a much more gradual slope of $m_{nuc} \propto 0.90(\pm 0.17) m_{gal}$ for g-band galaxies.

They also report an average nucleus-to-galaxy light ratio of $\langle \eta_g \rangle = 0.37\% \pm 0.04\%$. We find this in our sample to be $\langle \eta_g \rangle = 0.83\%$. We also find a very similar average for the r-band image; $\langle \eta_r \rangle = 0.82\%$. These averages are however not entirely comparable, as, like den Brok et al. (2014), Turner et al. (2012) use HST data, and their method of obtaining central magnitudes was different from ours, taking the central most 4 pixels and using aperture photometry. Again we can conclude that our nuclei are unresolved, and that the different methods introduce some offset between the samples.

4.4 Kormendy relations

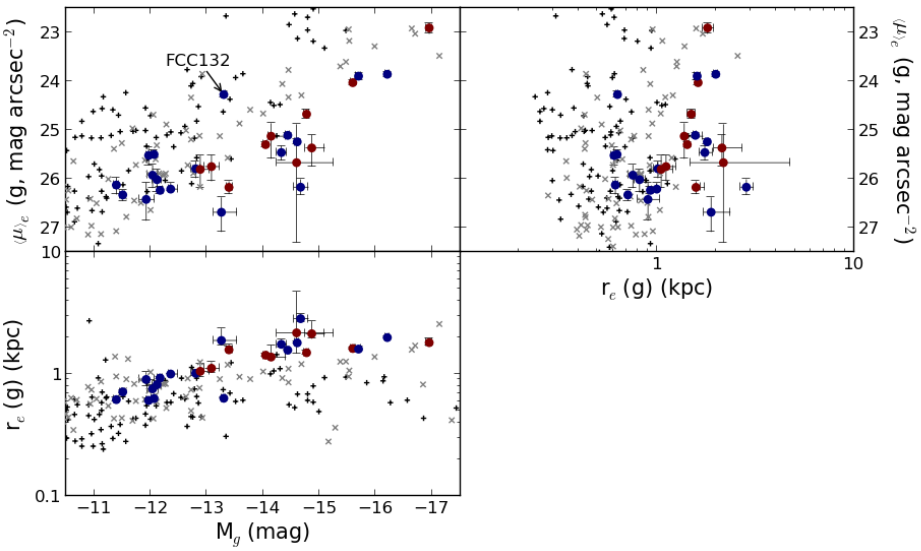

Figure 4.5: *Global parameter correlations: g'-band magnitude (M_g), r_e (g') and $\langle\mu\rangle_e$ (g'). Red circles are nucleated galaxies, blue circles are non nucleated. Overplotted is data from Misgeld et al. (2008) (+) and Misgeld et al. (2009) (×) from the Hydra I and the Centaurus cluster, respectively.*

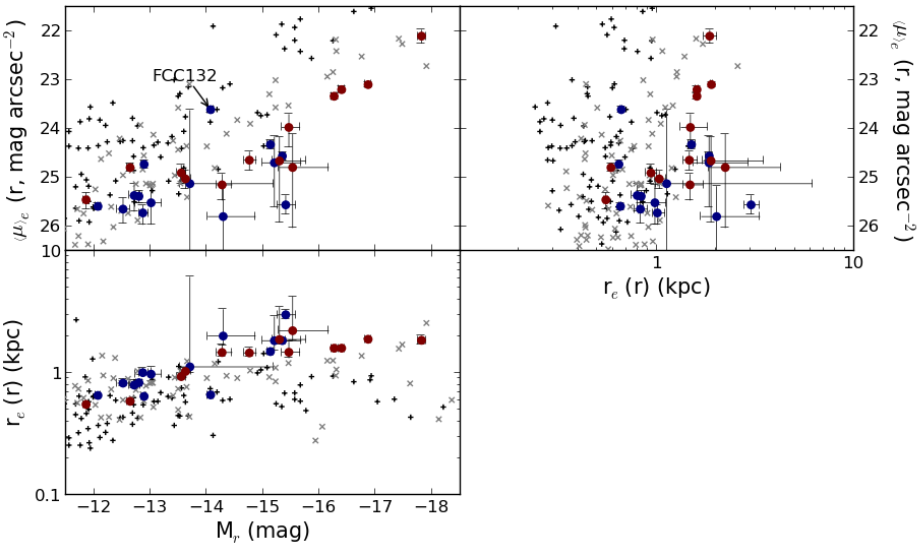

Figure 4.6: *Global parameter correlations: r-band magnitude (M_r), r_e (r') and $\langle\mu\rangle_e$ (r'). Markers are the same as in figure 4.5*

The Kormendy relation, as first coined by Kormendy (1977), is the relation between the surface brightness of a galaxy and its size (effective radius), where the surface brightness decreases with

increasing size. We will first review the relation between surface brightness and galaxy luminosity, and then see whether the same type of correlation can be found with respect to r_e. We will then compare our results with studies from recent literature, and look deeper into the one clear outlier, FCC132.

In figures 4.5 and 4.6 we show the parameter space spanned by the radius, magnitude and surface brightness parameters in both g' and r'. The correlation between surface brightness and magnitude is clear: brighter galaxies have higher surface brightness. The correlation between effective radius and absolute magnitude is also visible, albeit less pronounced than the former. We note that these parameters, and especially SB, are not independent as r_e and magnitude were both fitted simultaneously, and SB was derived from these two parameters. Regardless, there does not seem to be a clear correlation between r_e and SB , since r_e remains roughly constant over a large range of SB. On average the larger galaxies tend to have slightly brighter SBs, but the spread is large. We also see this for the dSphs in Kormendy et al. (2009).

Mieske et al. (2007) find a slope of $\mu_{V,0} \propto 0.681\mathrm{M}_{V,0}$. This slope is roughly equivalent to our fitted slope of $\langle\mu_g\rangle_e \propto 0.48\mathrm{M}_g$. Although the effective radius of a galaxy seems to depend less on galaxy magnitude when going to the brighter regime, our linear scaling relation seems to underestimate the surface brightness at the bright ($\mathrm{M}_g < -16$) end, and overestimate the surface brightness at the faint and intermediate end ($\mathrm{M}_g > -16$).

When observing the $\log(r_e)$-M relation in g', we find that $\log(r_e) \propto -0.10\mathrm{M}_g$. In g' and especially r', we see that a linear fit in these parameters may not suit the data optimally. Alternatively, the $\log(r_e)$-M relation might benefit from a slightly steeper slope at the faint end. Misgeld et al. (2009) report a linear relation over their large magnitude range of $-21 < \mathrm{M}_V < -10$, but their fit may benefit as well from two different slopes or a constantly varying slope. Their reported slope over this magnitude range is $\log(r_e) \propto -0.041\mathrm{M}_V$. They do also report a steeper slope of $\log(r_e) \propto -0.107\mathrm{M}_V$ for Local Group dwarf galaxies with $\mathrm{M}_V > -13$. This means that our retrieved relation is more consistent with the faint end than the bright end.

Janz and Lisker (2008) find only a gradual slope with effective radius and magnitude. Unfortunately, no comprehensive comparison is possible as there is no online data available for their galaxies.

We note one clear outlier, FCC132, which has an unusually high surface brightness for its magnitude compared to the rest of the sample. Similar high SB objects were also observed in the Centaurus cluster by Misgeld et al. (2009), and are denoted as candidate compact ellipticals (cEs). Like their C-1-21 galaxy, this galaxy has a $\sim$2 magnitude brighter surface brightness than other galaxies in its magnitude range. We further look into this in section 5.1.

Hoyos et al. (2011) report a trend where brighter galaxies tend to have brighter SBs as well (their figure 12). We find that our galaxies follow the same trend. Our highlighted outlier, FCC132, would be just on the edge of their proposed parameter space.

4.5 Colours

4.5.1 Global colours

In figure 4.7 we show the total galaxy colours as found in this study, plotted together with the results from Venhola et al. (2017, *in prep.*) and Kim et al. (2010). Fitting the points with a line gives the following relation:

$$(\mathrm{g'\text{-}r'}) = -0.034\mathrm{r'} + 1.31, \tag{4.3}$$

whereas Venhola et al. (2017, *in prep.*) report $(\mathrm{g'\text{-}r'}) = -0.035r + 1.26$ and Kim et al. (2010) report $(\mathrm{g'\text{-}r'}) = -0.04R + 0.04$, which at a distance modulus of $m - M = 31.51$ (Blakeslee et al., 2009) translates to $(\mathrm{g'\text{-}r'}) = -0.04r + 1.30$. Both these relations are also plotted in figure 4.7.

All three slopes are very similar. Our sample is on average slightly redder than both the sample from Venhola et al. (2017, *in prep.*) and Kim et al. (2010). We see that our galaxies are on average slightly brighter than those of Venhola et al. As our galaxies are on average slightly brighter than the sample of Venhola et al. (2017, *in prep.*), this might be due to an non-linear colour change in

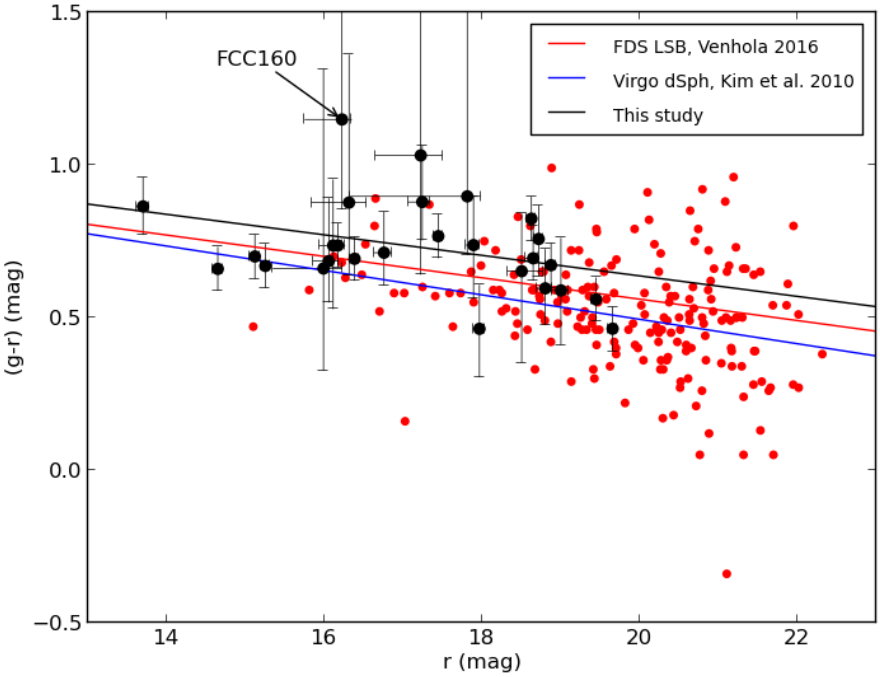

Figure 4.7: *(g'-r') colour-magnitude diagram of the FDS LSB sample by Venhola et al. (2017, in prep.) (red), the derived relation from Kim et al. (2010) (blue) and this study (black).*

(g'-r') with magnitude, also noted before by eg. Ferrarese et al. (2006); Janz and Lisker (2009). The dSphs from Virgo, as studied by Kim et al. (2010), are morphologically comparable to our sample. Our fit agrees with theirs within 2σ confidence intervals.

Because of its position in the colour-magnitude diagram, we looked into literature to find other colour estimates for the galaxy FCC160. Mieske et al. (2007) report global colours of FCC160, with $(V-I)_0 = 0.99$, which deviates from their reported trend of $(V-I)_0 \propto 0.033\mathrm{M}_{V,0}$ by only $\sim$1%, so it is not known to be especially red from literature. However, the error on the measured colour is quite large, allowing also a less red colour that would agree with the derived relation.

Sánchez-Janssen et al. (2016) report a best-fit (g'-i') colour magnitude relation of (g'-i')$\propto -0.33\mathrm{M}_g$ for a sample of low luminosity Virgo cluster members. This is very close to our (g'-r') slope.

4.5.2 Central colours

In figure 4.8 we show our central (g'-i') colour (from aperture photometry) compared to (g'-i') central colour as reported by Turner et al. (2012). Data from Turner was converted from z'-band magnitudes to i'-band magnitudes by a conversion factor of (i'-z') = 0.36 (Fukugita et al., 1995). No galaxies match amongst our sample and theirs, so a direct comparison was not possible.

As can be clearly seen, the trend that Turner et al. (2012) report cannot be observed in our galaxies, which lie in the fainter regime. Their reported slope is too steep to match our data. We believe this is due to contamination from the underlying galaxy in our sample. Our nuclei remain unresolved at the distance of Fornax, so we inevitably introduce some galaxy light in our central colours. With the large scatter in the data by Turner, the fit they present is up for debate. When combining the fainter end of their sample and the data from our sample, it is possible that for faint Fornax dwarfs the (g'-i') nucleus colour becomes independent of total galaxy luminosity.

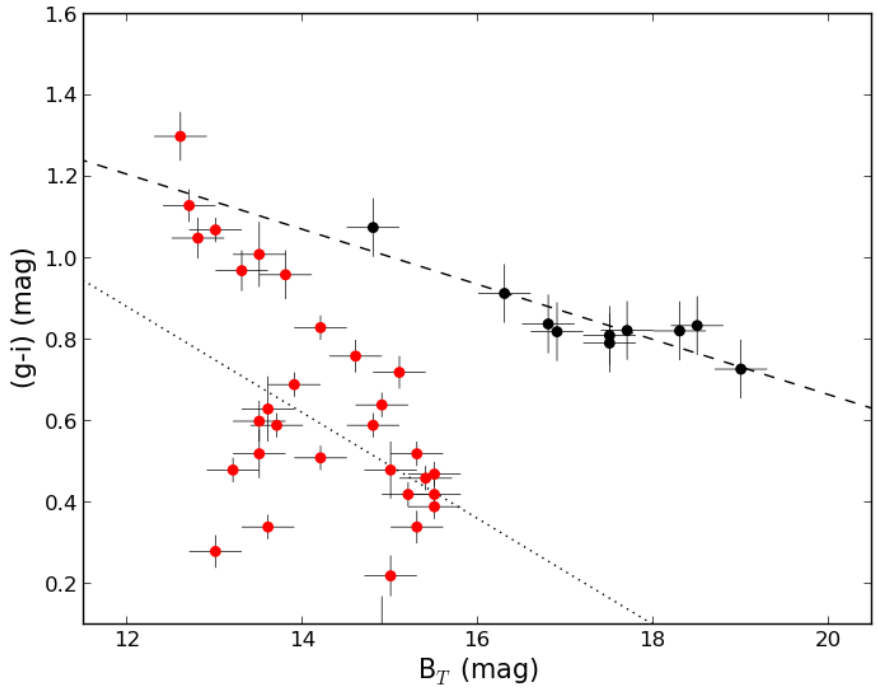

Figure 4.8: *Central g'-i' colours of Turner et al. (2012) (red) plotted together with data from this study (black) against their B_T-band magnitude as reported in Ferguson (1989) (our data) or from Glass et al. (2011) for Turner. Dotted line is best fit from Turner et al. (2012) for galaxies with $B_T \geq 13.5$, dashed line is our best fit. Errors in B_T are standard ± 0.3, errors in our sample are combined standard minimum errors (as reported in section 2.1, ± 0.04 for g', ± 0.06 for i'), errors in Turner are as reported therein.*

Rather than a trend with magnitude, it shows a spread around a constant value. To assess this, more nuclei of galaxies with $B_T > 15$ should be studied.

4.5.3 Nucleus and global colours

To study the possible differences in stellar population between the central parts and the outer parts of the galaxy, we plot in figure 4.9 the (g'-i') and (g'-r') colours of the total galaxy and the central regions of all galaxies (top), as well as the difference in colour as a function of galaxy magnitude (bottom).

The retrieved colour for central region and galaxy can be quite different. Overall, we do not see explicit trends. We find that the overall galaxy (g'-i') colour does not change significantly over the whole range of magnitudes, but the spread is quite large. The central regions of the galaxies in this colour do seem to turn towards bluer for the fainter galaxies. In the (g'-r') colour we the opposite. The fit for the central colours against the host magnitude remains very constant, whereas the galaxies seem to turn slightly to the blue for fainter galaxies. We find that for both colours, roughly half of the sample galaxies' central regions are bluer, and half are redder.

The overplotted least square fits from figure 4.9 for the (g'-i') colour are

$$(\text{g'-i'})_{gal} = -0.006\text{g'}_{gal} + 1.00, \tag{4.4}$$

$$(\text{g'-i'})_{nuc} = -0.031\text{g'}_{gal} + 1.43, \tag{4.5}$$

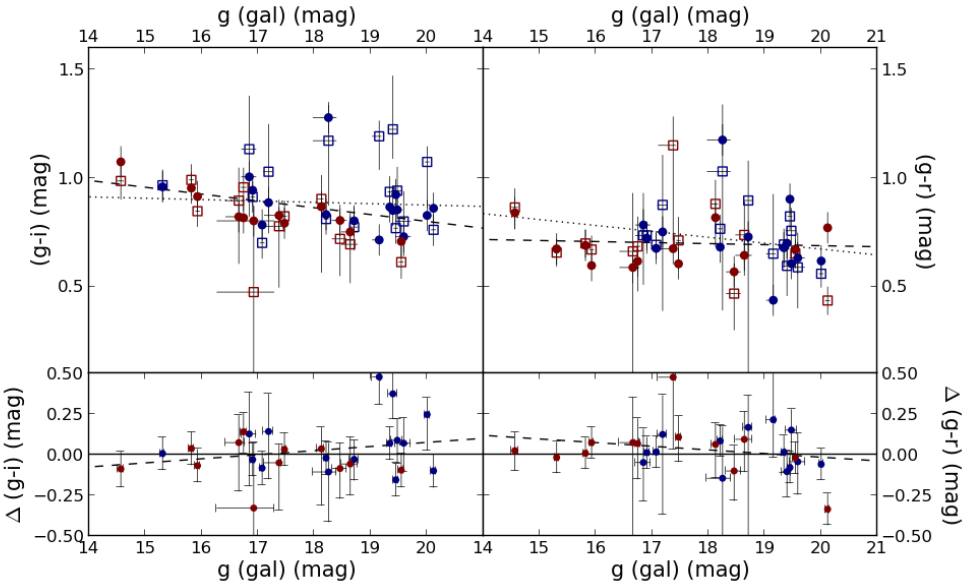

Figure 4.9: *Colours and colour relations for all sample galaxies. Top: galaxy colours (squares) and nucleus colours (dots) with their linear best fit relations, plotted against galaxy g-band magnitude. Dotted lines are best fits for the galaxies, dashed lines are best fits for the centers. Bottom: colour difference between galaxy and nucleus, with the dashed line its best fit. All central colours taken with aperture photometry, all galaxy colours from Galfit-models. Red data points are nucleated galaxies, blue are non-nucleated.*

and

$$\Delta(\text{g'-i'}) = 0.025\text{g'}_{gal} - 0.43. \tag{4.6}$$

For the (g'-r') colour these are

$$(\text{g'-r'})_{gal} = -0.027\text{g'}_{gal} + 1.22, \tag{4.7}$$

$$(\text{g'-r'})_{nuc} = -0.005\text{g'}_{gal} + 0.78, \tag{4.8}$$

and

$$\Delta(\text{g'-r'}) = -0.022\text{g'}_{gal} + 0.43. \tag{4.9}$$

Because of the flat slopes of the relations, the spread around the relations and the relatively large errors, we cannot draw conclusions on the difference in colour-magnitude relations (central and total) for this sample of dwarfs. The presence of a nucleus does not seem to influence the central regions' colours towards the blue or red significantly. We will discuss the topic of central colours further in section 5.3.

4.6 Sérsic-index

The Sérsic index (Sérsic, 1968) is a parameter that determines the shape of the light profile of a galaxy (see equation 3.6). Classically, for giant ellipticals this parameter is expected to be $n \approx 4$ (de Vaucouleurs' law), and for dwarfs $n \approx 1$ (an exponential profile). The higher the index n, the more light is concentrated in the central parts of the galaxy. In this section, we will compare the Sérsic indices of galaxies in our sample galaxies with recent results from the Fornax Cluster by Venhola et al. (2017, *in prep.*).

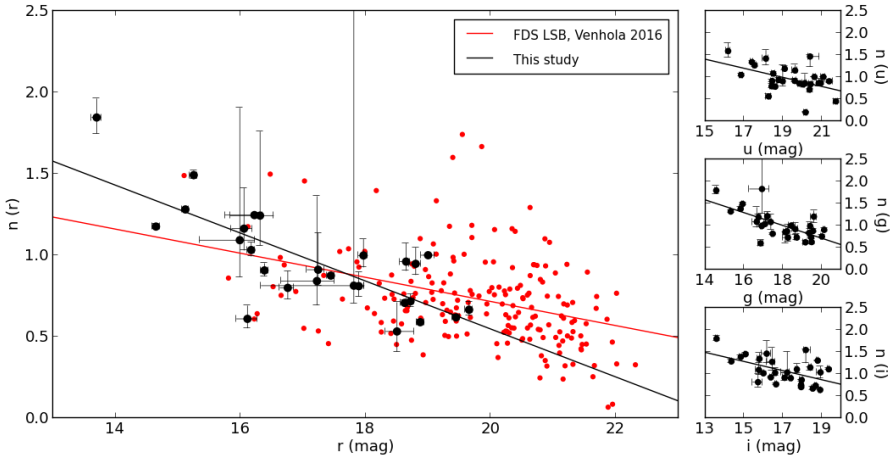

Figure 4.10: *Left: Sérsic-index plotted against best fit r-band magnitudes. Shown is also the galaxies and best fit from Venhola et al. (2017, red). Right, from top to bottom: Sérsic-index plotted against u'-, g'-, and i'-band magnitudes, respectively. Errorbars are derived from best-fit models with adjusted background levels.*

4.6.1 Sérsic-index as a function of magnitude

As can be seen in figure 4.10, there is a positive trend between Sérsic-index and brightness. As expected, the brighter galaxies tend to have higher Sérsic-indices. This effect seems more pronounced near the bright end of the sample. This might suggest that the brighter galaxies are more similar to giant elliptical galaxies than to dwarfs. For g'-band images we get the following linear relation:

$$n_g = -0.15\text{g'} + 3.6, \tag{4.10}$$

and for r-band galaxies, its

$$n_r = -0.15\text{r'} + 3.5. \tag{4.11}$$

If we compare this to the results of Venhola (2017, private conversation) as shown in figure 4.10, we see that the slope of the fit is not drastically different for the fainter sample of Venhola then for our sample. A linear fit of their data reports

$$n_r = -0.073\text{r'} + 2.2. \tag{4.12}$$

This could lead to believe that the slope of the Sérsic index as a function of magnitude decreases as we move to fainter magnitudes and levels around $n \approx 0.5$. There is no underlying physical concept why the relation should be linear. The constraint of $n > 0$ could well lead to asymptotic behaviour at the faint end.

When studying the results of den Brok et al. (2014), we find that they also report a correlation between Sérsic index and brightness, but fit a logarithm to their results and fit n to the nucleus magnitude rather than a total magnitude. They find $\mathrm{M}_{F814W} = (-5.2 \pm 0.7)\log_{10}(n/3) - (12.6 \pm 0.3)$, where M_{F814W} is the nucleus magnitude. Although they do also find a positive correlation between nucleus brightness and Sérsic index (and thus galaxy brightness and n, see section 4.3), the scatter is quite large.

Chapter 5

Discussion

In this chapter we will highlight some of our results in the light of their (possible) physical origins, explain certain discrepancies, go over the limitations of our research and finally make recommendations for further research.

5.1 Kormendy relations

As we have noted in section 4.4, we find that both the $\log(r_e)$-M relation and the M-SB relation can be well approximated by linear fits. These are indications that the average size does increase with surface brightness, but the spread is large. That being said, the magnitude-size relation of the galaxies in our sample would benefit from a varying slope, with increasing steepness for fainter galaxies. This is consistent with results from Misgeld et al. (2008, 2009) and can also be seen in figures 4.5 and 4.6. From this and the interdependence of our parameters, we find that a steeper slope for the magnitude-surface brightness at the bright end might be more appropriate. These findings are consistent with the results that Misgeld et al. (2009) find over a large magnitude range for a sample of galaxies from the Centaurus cluster (at the bright end) and the Local Group (at the faint end). As their slope of the size-luminosity relation for giant ellipticals is steep, this would result in an 's'-shaped magnitude-size relation for the whole family of ellipticals, as also proposed by Janz and Lisker (2008). This can be seen in figure 5.1. In this figure we expanded the plotted range to include all galaxies from the Misgeld et al. (2008, 2009) papers. The percieved s-shape in the size luminosity diagram is an indication of different formation scenarios for giant- and dwarf ellipticals.

The size-surface brightness relation for our sample only follows a very weak trend with a large spread. As such, we cannot provide additional evidence for or against the proposed dSph/dE dichotomy (Kormendy et al., 2009). Because of the low upper limit on magnitude, we only find one galaxy that might be bright enough to be classified by Kormendy et al. (2009) to be a dE-type galaxy, which is clearly not enough to show a clear distinction in retrieved parameters.

The one clear outlier from the luminosity-surface brightness relation of our sample, FCC132 (see figures 4.5 and 4.6), can be considered a UCD-candidate. Its surface brightness is ~ 2 magnitudes brighter than what is expected for galaxies with its total luminosity. These types of objects are also seen in the Centaurus cluster study by Misgeld et al. (2009), showing the most similarities to their 'C-1-21' galaxy. As cE galaxies could be considered low mass counterparts to giant ellipticals (Kormendy et al., 2009), UCDs may be the low mass counterparts to dwarf ellipticals. They may form if they were compact at the time of their formation (Misgeld et al., 2009) and lost their envelopes in interactions. Another formation scenario is through galaxy 'threshing' (Bekki et al., 2001), meaning that they were originally at higher luminosity and radius and may be the remnant central part of an ordinary dwarf elliptical that has been tidally stripped of its outer parts by multiple passes past a large galaxy. Because FCC132 is still on the faint side of the surface brightness spectrum when it comes to UCD, it should be considered a slightly deviating

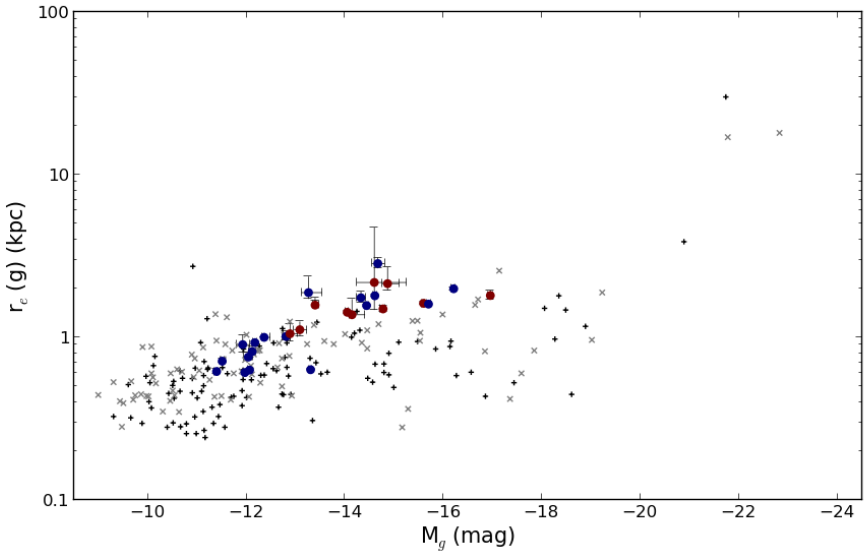

Figure 5.1: *Same as the bottom image in figure 4.5, but with extended magnitude and size ranges to include the full sample of Misgeld et al. (2008, 2009).*

but still 'normal' dwarf elliptical. It is simply not bright or compact enough to be considered a UCD galaxy.

5.2 Sérsic index

As mentioned in section 4.6, n is a measure of the light profile shape of a galaxy. For dwarf galaxies this parameter is often estimated to be close to 1. We find in the aforementioned section that our values of n vary between 0.5 and 2, which, as mentioned, is what is to be expected from dwarfs (Caon et al., 1993). We find a slope with galaxy magnitude that indicates smaller n for fainter galaxies. Also, we see that our slope for our slightly brighter sample is steeper than for the LSB sample of Venhola et al. (2017, *in prep.*). This indicates that over a large range of magnitudes, perhaps a logarithmic fit (as in den Brok et al., 2014) would provide a better estimate compared to our linear fit. We cannot confirm a logarithmic fit in this study, as we do not have the needed luminosity range in our sample. We see that the typical errors on the Sérsic index are smaller than their offset from the found trend. Though partly this may be because of inaccuracies from the linear fit, this also suggests that there is some natural spread in n that does not arise from the overall luminosity of the galaxy. Therefore, environmental effects are expected to play a role in the evolution of each dwarf galaxy.

What we can also clearly see from figure 4.10 is that the slope of the $n-$M relation does not vary significantly between the different bands. All slopes show a similar increase in n with increasing brightness, and they all show a similar spread around the linear fit.

Mahajan et al. (2015) report that they find a correlation between n and M for larger galaxies (giant ellipticals) but do not see the same trend continue into the dwarf galaxy regime ($M_Z > -18$). Therefore they state that it is not very useful to classify dwarfs by their Sérsic index. Although it may be true that the spread in n becomes very large for fainter galaxies and is thus not very useful in determining general properties of the dwarf, it may still be a useful parameter to look at the influences of the environment for each individual galaxy.

5.3 Central regions

Our measurements seen in sections 4.5.2 and 4.5.3 show that around half of our galaxies show blue regions in their central parts. This means that these central regions contain on average more young, blue stars than the outer parts. In this section we will review how our findings compare with recent literature.

Pak et al. (2014) studied the properties of early-type galaxies in the Ursa Major cluster. They find that $\sim 70\%$ of their early type dwarf galaxies show evidence of central star formation, based on these galaxies exhibiting central colours that are bluer than their outer parts. The reported offsets are regularly more than 0.2 mag, which is something that we see in our sample as well (eg, figure 4.9).

This finding, as well as ours, is in stark contrast to the study of Lisker et al. (2006) of early-type dwarf galaxies in the Virgo cluster, who find only $\sim 5\%$ of such blue-cored galaxies. They also conclude that the percentage of blue-cored dwarfs declines to $\sim$0% for $m_B > 16$, a feature that we do not see in our Fornax cluster sample. Though nucleation decreases with magnitude, this might simply be down to selection effects stemming from lower S/N ratios for fainter galaxies, rendering the detection of their nuclei increasingly difficult with decreasing luminosity. Pak et al. (2014) concludes from this, as well as from the results of De Rijcke et al. (2013) and Lisker et al. (2006), that low density environments are very favourable for blue-cored early-types dwarf galaxies to form. While this may be true, in this study we see that these blue center dwarfs also exist towards the central, denser parts of the Fornax cluster.

More recently, Hamraz et al. (2017, *in prep*) have also found blue colours in the central regions in a sample of Fornax galaxies, with varying radial distance from the cluster center. They find that their sample has a blue-core percentage of $\sim$73%. They also study a similar sample in the Virgo cluster, and find a blue-core percentage of $\sim$57%. In their study, they find that the blue regions of these galaxies extend to around 0.3" to 0.5". Beyond this inner radius, the galaxies' colours are found to be much redder compared to the center. Our FWHM is larger than these radii, which makes it probable that we are underestimating the blue-core percentage in this study. Taking into account offsets in colour with the accuracy of our measurements, it is doubtful whether there really is a colour difference between regions within an $\sim$1.3" radius (the low limit on the FWHM) and the rest of the galaxy, or whether any colour offset has been hidden by the galaxy light.

We find that $\sim 50\%$ of our galaxies are bluer in their central regions than in the rest of the galaxy. Though our errors are relatively large and our data is not as deep as the Fornax study of Hamraz et al. (2017), the Coma cluster study by den Brok et al. (2011), and the Ursa Major cluster studied by Pak et al. (2014), we believe that from this result we can conclude that the method used by Lisker et al. (2006) does not yield a representative result of the blue-core early-type dwarf galaxy percentage in Virgo, and definitely not of the complete dwarf galaxy sample across these clusters.

But what formed these blue centers? Several scenarios have been suggested in recent literature. One of these is ram pressure stripping of the outer regions of dwarf irregulars (dIrr) or even giant spirals. The theory is that as these galaxies traverse the intracluster medium, they are stripped of the gas in their outer regions, triggering star formation in its center (). This would mean that galaxies in denser regions should have bluer centers. Another theory is that the dwarf galaxies have undergone galaxy harassment; encountering massive galaxies (fly-bys) that disrupt the morphology of the galaxy, as well as mixing the remaining gas of the galaxy. This could lead to a new star formation episode (Lisker et al. (2006), Turner et al. (2012), den Brok et al. (2014)). Because most of our galaxies are relatively isolated from giant companions, this is probably not the cause of the bluer centers.

5.4 Direct comparison with Muñoz et al. (2015)

In this section we will discuss the results of the paper by Muñoz et al. (2015). They study Fornax in the u'-, g'-, and i'-bands and theirs and our sample have some overlap. Therefore it is instructive

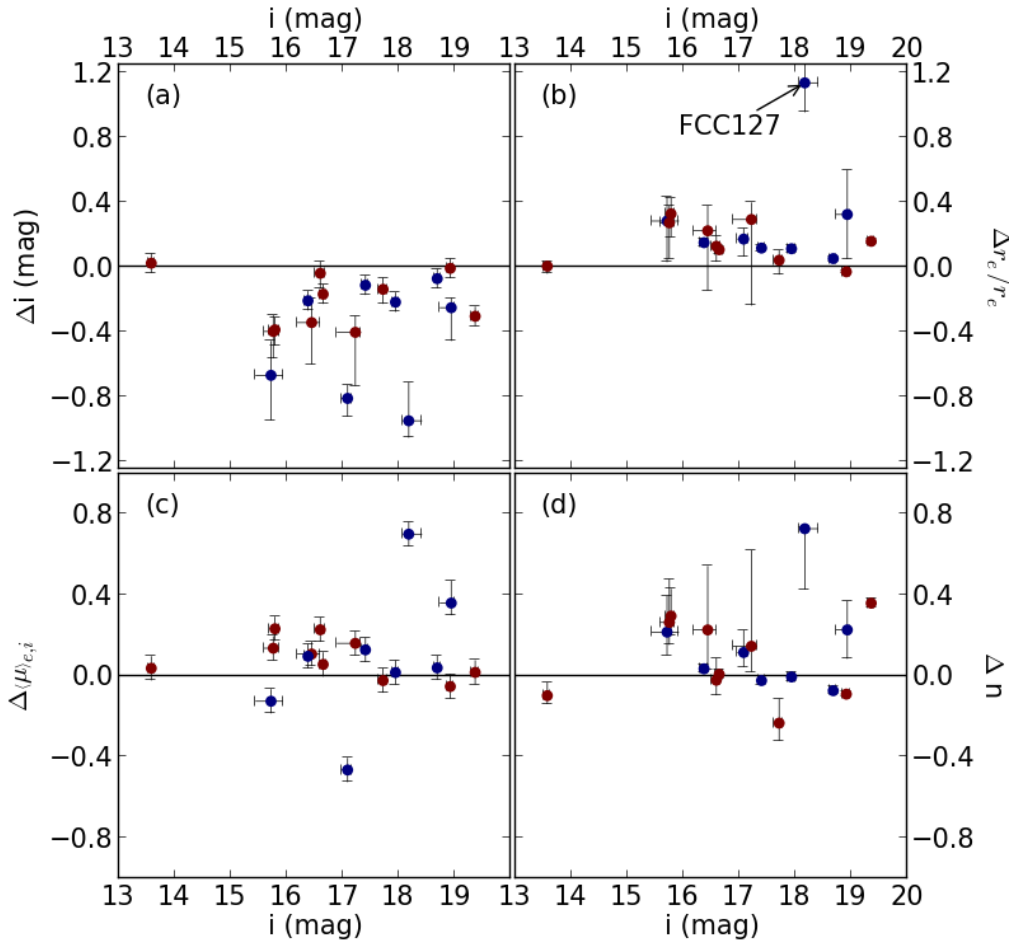

Figure 5.2: *(a) Difference in galaxy magnitude between Muñoz et al. (2015) and our coinciding galaxies:* $\Delta i' = i' - i'_{Munoz}$*. (b) Difference in* r_e *for aforementioned galaxies, divided by* r_e *from Munoz. (c) Difference in effective surface brightness. (d) Difference in retrieved Sérsic index. All errors are only from our best-fit models, and do not include error estimates from Muñoz et al. (2015) because they remain unmentioned therein.*

to compare the common galaxies between the two surveys. The results of these comparisons are found in figure 5.2.

It is clear that the results are not a good match. If we look at figure 5.2(a), our galaxies are on average ~ 0.3 magnitudes brighter than their retrieved value from Muñoz et al. (2015) for the same galaxies, in the same band (in this case, the i'-band). Venhola et al. (2017, *in prep.*) also report an offset of $\sim 0.3 \pm 0.3$ mag. An offset is also clear in the following figures, though the mean offset in surface brightness and n are closer to $\Delta \approx 0$ than for i' and r_e. The offset in radius increases with increasing luminosity, with the exception of the brightest galaxy in the sample (FCC136) and the clear outlier of FCC127. What is clear though is that the offset is in the positive direction for all but one galaxy, meaning that we find larger radii than Muñoz et al. (2015) do.

Thesurface brightness more or less centers around $\Delta = 0$. This is probably due to the surface brightness dependence on both r_e and m and the trade off between these parameters when modeling using Galfit. Because of this parameter entanglement, the offsets in r_e and m cancel each other

out. The offset in n is, bar three clear outliers in the fainter end of the sample, not very large. As Muoz et al. (2015) do not specify error estimates, the discrepancies we find could however be overestimated. To look for possible differences, we will now analyze their methods.

Muñoz et al. (2015) use a very similar method to our own. They create individual postage stamps for all galaxies, and mask any bad pixels and non-dwarf sources. Subsequently, they perform fits using Galfit, which are then classified as nucleated or non-nucleated. The process of this classification is not stated. For the non-nucleated galaxies they fit a single-Sérsic profile. For the nucleated galaxies they use two components. Where their method deviates from ours, is that they keep the initial guess for the magnitude (retrieved from Sextractor Bertin and Arnouts, 1996) fixed. They then fit again using the retrieved parameters as input, but keeping all parameters apart from the magnitude fixed. This process of fixing and fitting is then repeated one more time.

In the aforementioned method, the initial guess has a larger weight in the final determination of the parameters than what may be desirable. Especially low luminosity objects like dwarf galaxies are very sensitive to minor adjustments in parameters, which can have quite substantial effects on other parameters. Because of the low surface brightness of these objects, the residuals of the galaxies (as provided by Galfit) can visually seem homogeneous with very divergent parameters. Arguably, a more accurate fit could be obtained by a fully free fit. Especially for non-nucleated galaxies with one component to fit, this should be possible, as we have indeed shown in this thesis. In the case of nucleated galaxies, they first masked out the nucleus and derived the global galaxy parameters. Then, all but the nucleus was masked out and the central regions of the galaxy were fit. This however fails to make use of one of the strenghts of Galfit; its capability to model multiple components of multiple sources at once. We cannot check the parameters of these inner profiles as they are not disclosed in the paper.

Only one galaxy was found by Muñoz et al. (2015) to have a nucleus whereas in our sample it is classified as non-nucleated in the i'-band image. This galaxy (FCC131, seen in figure 5.3) however is found to be nucleated in our r'-band data. Muñoz et al. (2015) do not report their seeing limitations.

FCC131 has a bright feature slightly north ($\sim$ 1") of the galaxy photocenter. It is therefore debatable whether this is a nucleus of the galaxy or whether it is another object that simply happened to be in the line of sight. The orientation of the supposed nucleus is off by $\sim 50°$. This possible nucleus did not interfere with fits in the other bands (as it is less bright in u', g' and i'), and thus there was no need to add an extra profile to the fit. Even in the r'-band fit, the influence of the added Gaussian was minimal. While Muñoz et al. (2015) classify this object as a galaxy nucleus, we do not. We do however acknowledge the possibility that the galaxy contains an off-center nucleus. These are not entirely uncommon, as there have been reports of off-center nuclei in literature, for example Lisker et al. (2006); den Brok et al. (2014).

5.5 Limitations of this study

Though we believe that the parameters derived in this study are representative of the full dwarf population of Fornax, we must not forget that this analysis is a small selection of the fully available Fornax dwarf galaxy sample, limited to intermediate distances to the cluster center.

Due to the FWHM limitations of our data, it is difficult to study the central regions of dwarf galaxies in detail.

Further parameters that could be investigated include galaxy orientation in the sky, axis-ratios and overall position in the cluster. These parameters in particular could be used to constrain the environmental influences on the dwarfs. We note that Venhola et al. (2017, *in prep.*) does not find a strong depedence between the distance from the cluster center and galaxy colour or Sérsic index the sample of Fornax LSB galaxies.

Finally, we are limited by our sample size of 28. This allowed for very meticulous parameterization of these galaxies, but limits the accuracy of the derived relations.

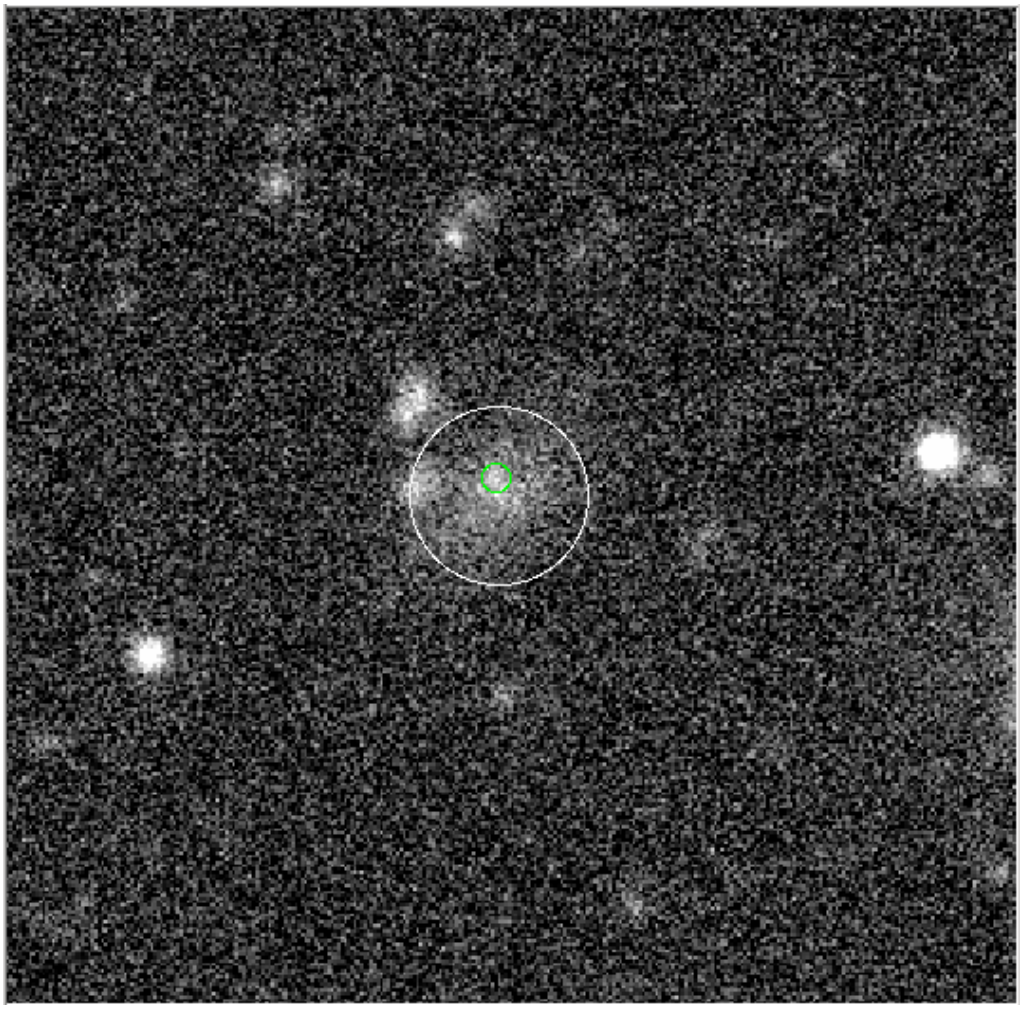

Figure 5.3: *i'-band image of FCC131, $\sim$ 65" by 65" scale. The supposed nucleus is found $\sim$ 1" up from the perceived photocenter in the green circle. The white circle denotes $r_e$around the photocenter.*

5.6 Recommendations

Though in the central parameters of Galfit fits were not used directly in this study, it would be good to set the FWHM of the Gaussian component in Galfit to the determined FWHM of the PSF, as this is a limiting factor in our analysis. This would enable us to better compare the results to the results of aperture photometry and furthermore enable a consistent comparison of all galaxies.

Clearly it would be interesting to extend the sample from just this field 16 to all dwarf galaxies in Fornax, by similarly parameterizing the dwarfs in other fields as well. This data was not available at the beginning of this project, but has since been completed. This will give a better basis to draw conclusions on the environmental effects of the Fornax Cluster on the dwarfs and provide more statistical power.

Visually inspecting our full images, we find a number of small or low surface brightness objects, not classified in the Ferguson Cluster Catalog. Studying these objects, we would be able to extend the trends into even fainter regimes. These objects are now being studied by Venhola et al. (2017, *in prep.*).

To achieve more consistent results across bands and therefore be able to make a more accurate

comparison between galaxy parameters, it is advisable to correct for seeing variations.

We think that the study of blue centers with high resolution imaging may be extended also to galaxies that have no clear nucleus. This may find a clear distinction between nucleated or non-nucleated galaxies, confirm that seeing effects are the main reason we don't find more nucleated dwarfs, or find that they have very different origins, for example their merger histories.

Chapter 6

Conclusions

We model a total of 28 dwarf galaxies from the FCC in four SDSS bands: u', g', r' and i'. Their magnitudes range between 16.2 and 21.7 in u', 14.6 and 20.1 in g', 13.7 and 19.7 in r', and 13.6 and 19.4 in i'. The results from aperture photometry and modeling using Galfit are in good agreement with each other, as well as in reasonable agreement with the Fornax Cluster Catalog by Ferguson (1989).

A nucleation percentage of 29%, 36%, 48% and 43% is found in u', g', r' and i', respectively. Out of these, a total of 7 galaxies show nucleation in all four bands, amounting to 25%. Brighter galaxies are more likely to have nuclei and their nuclei are found to be brighter, but the nucleus-to-galaxy luminosity ratio increases for fainter galaxies.

Both the magnitude-size relation and the magnitude-surface brightness relation can be well approximated by a linear fit for our sample galaxies. It is possible we are looking at the faint end of an 's' shaped magnitude-size relation across the whole spectrum of ellipticals, suggesting that there are different formation scenarios for giant- and dwarf-ellipticals. Our relations align well with previous findings. We find that FCC132 might be an outlier of the magnitude-surface brightness relation with a similar offset like the UCDs from Misgeld et al. (2009), but it is deemed too faint in $\langle\mu\rangle_e$ to be a UCD.

We find that though not all galaxies are nucleated and have a need for an extra fitting parameter, $\sim$50% of our sample galaxies have bluer centers than their outer regions. We cannot find a statistically reliable relation for the difference in global and central colours with magnitude, as the measurements of the central magnitudes experience too much contamination from the underlying galaxy.

For nucleated galaxies, the central colours are redder than expected from the observed trend from the brighter Fornax sample of Turner et al. (2012), which is probably the result of contamination in our sample from the underlying galaxy of each nucleus. The global colours are also slightly redder than similar studies by Venhola et al. (2017, *in prep.*) (LSB's in Fornax) and Kim et al. (2010) (dSphs in Virgo).

Sérsic indices increase with increasing luminosity. A linear fit is appropriate for our luminosity range, but comparing the results with Venhola et al. (2017, *in prep.*) and den Brok et al. (2014) we find that for the full luminosity range of ellipticals, an exponential may provide a better fit. The scatter in n is larger than our proposed errors, so we conclude that there is a natural spread in n with luminosity.

Our results are in good agreement with almost all relevant literature, but not with Muñoz et al. (2015). We believe their fitting procedure may have introduced unwanted bias towards their initial guesses, leading to these discrepancies.

Dwarf galaxies are a fascinatingly diverse group of objects, and in the coming years newly acquired data will allow further expansion of our knowledge of their parameters and origins.

Acknowledgments

I would like to thank my supervisor, prof. dr. Reynier Peletier for his support during my whole project and for the useful weekly discussions, where I learned a lot. I would also like to thank Aku for his contributions in getting me started and acquainted with the software and always being ready to answer my questions, even from faraway Finland. I am also thankful for the both the secretarial support and the support from the computer group. Furthermore, I would like to thank Lotte for her continuous support and believe in me. Even when things were not going as planned, she was there to give me what I needed, whether it was confidence, a nice warm meal or just a kick in the butt to get me going. Many thanks as well to Johanna, who was also vital in me getting my stuff together, as well as being a nice sparring partner for my troubles, a great housemate, an excellent choir mate, a thorough proof-reader and a good friend. Also I would like to thank Gerjon for his useful discussions, for showing me that finishing a masters can in fact be done, and to remind me that it really is time to graduate.

Appendices

Appendix A

Other tables

Table A.1: *Results for sample galaxies in the r'-band and galactic (u'-r') colour.*

Name	r' (mag)	$r_{e,r}$ (")	$\langle\mu\rangle_e$ (mag/"^{2})	n_r	(u'-r') (mag)	nucl.	r'$_n$ (mag)
(1)	(2)	(3)	(4)	(5)	(6)	(7)	(8)
FCC85	$15.25^{+0.05}_{-0.05}$	$16.4^{+0.3}_{-0.3}$	$23.33^{+0.05}_{-0.05}$	$1.49^{+0.03}_{-0.03}$	$2.29^{+0.03}_{-0.03}$	Y	$19.63^{+0.05}_{-0.05}$
FCC86	$16.31^{+0.48}_{-0.22}$	$18.9^{+11.0}_{-3.1}$	$24.69^{+0.51}_{-0.17}$	$1.24^{+0.52}_{-0.18}$	$2.19^{+0.48}_{-0.22}$	N	$21.26^{+0.05}_{-0.05}$
FCC93	$19.00^{+0.12}_{-0.10}$	$8.5^{+0.7}_{-0.5}$	$25.64^{+0.06}_{-0.05}$	$1.00^{+0.00}_{-0.00}$	$2.73^{+0.17}_{-0.15}$	N	$22.61^{+0.05}_{-0.05}$
FCC94	$18.72^{+0.06}_{-0.05}$	$8.6^{+0.4}_{-0.3}$	$25.38^{+0.05}_{-0.05}$	$0.72^{+0.05}_{-0.03}$	$1.71^{+0.08}_{-0.06}$	N	$22.87^{+0.05}_{-0.05}$
FCC97	$18.50^{+0.18}_{-0.27}$	$10.1^{+1.4}_{-1.2}$	$25.51^{+0.10}_{-0.05}$	$0.53^{+0.18}_{-0.12}$	$1.89^{+0.18}_{-0.55}$	N	$23.21^{+0.05}_{-0.05}$
FCC100	$14.65^{+0.05}_{-0.05}$	$19.5^{+0.3}_{-0.2}$	$23.09^{+0.05}_{-0.05}$	$1.18^{+0.02}_{-0.01}$	$2.20^{+0.03}_{-0.03}$	Y	$19.52^{+0.05}_{-0.05}$
FCC103	$18.65^{+0.10}_{-0.06}$	$10.4^{+1.0}_{-0.5}$	$25.72^{+0.10}_{-0.05}$	$0.96^{+0.11}_{-0.06}$	$1.39^{+0.11}_{-0.08}$	N	$22.43^{+0.05}_{-0.05}$
FCC110	$16.17^{+0.05}_{-0.05}$	$19.0^{+0.9}_{-0.7}$	$24.56^{+0.05}_{-0.05}$	$1.03^{+0.05}_{-0.04}$	$2.24^{+0.09}_{-0.08}$	N	$21.36^{+0.05}_{-0.05}$
FCC114	$19.44^{+0.05}_{-0.05}$	$6.7^{+0.1}_{-0.1}$	$25.58^{+0.05}_{-0.05}$	$0.62^{+0.01}_{-0.01}$	$1.63^{+0.13}_{-0.11}$	N	$22.82^{+0.05}_{-0.05}$
FCC116	$15.12^{+0.05}_{-0.05}$	$16.5^{+0.3}_{-0.3}$	$23.19^{+0.05}_{-0.05}$	$1.28^{+0.00}_{-0.00}$	$2.28^{+0.04}_{-0.04}$	Y	$19.86^{+0.05}_{-0.05}$
FCC123	$16.11^{+0.18}_{-0.15}$	$30.9^{+3.2}_{-2.3}$	$25.55^{+0.05}_{-0.05}$	$0.61^{+0.08}_{-0.06}$	$2.15^{+0.23}_{-0.21}$	N	$21.54^{+0.05}_{-0.05}$
FCC125	$17.81^{+1.48}_{-0.17}$	$11.6^{+51.7}_{-1.3}$	$25.12^{+2.21}_{-0.10}$	$0.81^{+1.76}_{-0.11}$	$2.55^{+1.49}_{-0.18}$	N	$22.57^{+0.05}_{-0.05}$
FCC127	$18.80^{+0.11}_{-0.08}$	$8.2^{+0.8}_{-0.5}$	$25.36^{+0.09}_{-0.06}$	$0.95^{+0.10}_{-0.07}$	$1.82^{+0.12}_{-0.09}$	N	$22.54^{+0.05}_{-0.05}$
FCC130	$17.22^{+0.58}_{-0.27}$	$20.7^{+13.6}_{-3.4}$	$25.79^{+0.52}_{-0.12}$	$0.84^{+0.52}_{-0.15}$	$2.94^{+0.58}_{-0.28}$	N	$23.33^{+0.06}_{-0.06}$
FCC131	$19.68^{+0.05}_{-0.05}$	$5.7^{+0.1}_{-0.1}$	$25.45^{+0.05}_{-0.05}$	$0.67^{+0.05}_{-0.04}$	$1.69^{+0.36}_{-0.21}$	Y	$22.38^{+0.05}_{-0.05}$
FCC132	$17.44^{+0.05}_{-0.05}$	$6.8^{+0.1}_{-0.1}$	$23.60^{+0.05}_{-0.05}$	$0.87^{+0.01}_{-0.01}$	$2.16^{+0.05}_{-0.04}$	N	$20.80^{+0.05}_{-0.05}$
FCC133	$-^a$	–	–	–	–	–	–
FCC136	$13.70^{+0.08}_{-0.07}$	$19.1^{+1.7}_{-1.3}$	$22.10^{+0.10}_{-0.08}$	$1.85^{+0.12}_{-0.10}$	$2.47^{+0.15}_{-0.12}$	Y	$18.12^{+0.05}_{-0.05}$
FCC137	$16.06^{+0.20}_{-0.13}$	$15.2^{+3.4}_{-1.6}$	$23.97^{+0.23}_{-0.11}$	$1.16^{+0.25}_{-0.13}$	$2.06^{+0.26}_{-0.18}$	Y	$20.64^{+0.05}_{-0.05}$
FCC140	$17.90^{+0.10}_{-0.08}$	$10.6^{+0.8}_{-0.6}$	$25.02^{+0.06}_{-0.05}$	$0.81^{+0.09}_{-0.06}$	$2.24^{+0.17}_{-0.10}$	Y	$21.58^{+0.05}_{-0.05}$
FCC142	$17.99^{+0.09}_{-0.07}$	$9.6^{+0.7}_{-0.5}$	$24.90^{+0.07}_{-0.05}$	$1.00^{+0.10}_{-0.07}$	$1.65^{+0.17}_{-0.13}$	Y	$21.43^{+0.05}_{-0.05}$
FCC144	$18.62^{+0.05}_{-0.05}$	$6.6^{+0.1}_{-0.1}$	$24.72^{+0.05}_{-0.05}$	$0.71^{+0.02}_{-0.02}$	$2.21^{+0.09}_{-0.07}$	N	$21.84^{+0.05}_{-0.05}$
FCC146	$18.89^{+0.05}_{-0.05}$	$6.0^{+0.1}_{-0.1}$	$24.79^{+0.05}_{-0.05}$	$0.59^{+0.01}_{-0.02}$	$2.05^{+0.05}_{-0.04}$	Y	$21.75^{+0.05}_{-0.05}$
FCC156	$16.38^{+0.05}_{-0.05}$	$15.4^{+0.7}_{-0.6}$	$24.32^{+0.05}_{-0.05}$	$0.91^{+0.04}_{-0.04}$	$2.06^{+0.07}_{-0.06}$	N	$21.35^{+0.05}_{-0.05}$
FCC157	$17.24^{+0.18}_{-0.10}$	$15.2^{+2.6}_{-1.1}$	$25.15^{+0.16}_{-0.06}$	$0.91^{+0.23}_{-0.10}$	$2.60^{+0.20}_{-0.12}$	Y	$21.91^{+0.05}_{-0.05}$
FCC158	$16.00^{+0.65}_{-0.24}$	$22.9^{+20.8}_{-3.9}$	$24.79^{+0.75}_{-0.17}$	$1.09^{+0.81}_{-0.23}$	$2.62^{+0.65}_{-0.25}$	Y	$20.42^{+0.05}_{-0.05}$
FCC160	$16.22^{+0.35}_{-0.12}$	$19.4^{+16.4}_{-1.7}$	$24.65^{+0.98}_{-0.07}$	$1.25^{+0.01}_{-0.01}$	$2.86^{+0.35}_{-0.14}$	Y	$21.21^{+0.05}_{-0.05}$
FCC165	$16.76^{+0.13}_{-0.10}$	$15.0^{+1.5}_{-1.0}$	$24.64^{+0.08}_{-0.05}$	$0.80^{+0.10}_{-0.07}$	$2.02^{+0.14}_{-0.11}$	Y	$21.32^{+0.05}_{-0.05}$

Notes. Column keys: (1) Galaxy name from the Fornax Cluster Catalog (Ferguson, 1989). (2) r-band magnitude as determined by Galfit (in magnitudes). (3) Effective radius in arcsec from Galfit-fitting. (4) Calculated effective mean surface brightness (in magnitudes per square arcsec). (5) Sérsic index. (6) Galaxy (u'-r') colour (in magnitudes). (7) Nucleated fit (Y) or non-nucleated fit (N). (8) r'-band central magnitude.

[a] FCC133 has no fit in the r'-band

Table A.2: *Results for sample galaxies in the i'-band and galactic (g'-i') colour.*

Name	i' (mag)	$r_{e,i}$ (")	$\langle\mu\rangle_e$ (mag/"^{2})	n_i	(g'-i') (mag)	nucl.	i'$_n$ (mag)
(1)	(2)	(3)	(4)	(5)	(6)	(7)	(8)
FCC85	$15.08^{+0.06}_{-0.06}$	$15.6^{+0.4}_{-0.3}$	$23.04^{+0.06}_{-0.06}$	$1.45^{+0.03}_{-0.03}$	$0.85^{+0.04}_{-0.03}$	Y	$19.33^{+0.06}_{-0.06}$
FCC86	$16.16^{+0.27}_{-0.21}$	$20.4^{+5.7}_{-3.5}$	$24.71^{+0.27}_{-0.20}$	$1.46^{+0.29}_{-0.22}$	$1.03^{+0.28}_{-0.22}$	N	$21.14^{+0.06}_{-0.06}$
FCC93	$18.79^{+0.06}_{-0.06}$	$9.1^{+0.1}_{-0.1}$	$25.58^{+0.06}_{-0.06}$	$1.31^{+0.01}_{-0.01}$	$0.80^{+0.15}_{-0.13}$	N	$22.51^{+0.06}_{-0.06}$
FCC94	$18.53^{+0.06}_{-0.06}$	$8.3^{+0.3}_{-0.3}$	$25.13^{+0.06}_{-0.06}$	$0.67^{+0.04}_{-0.03}$	$0.94^{+0.12}_{-0.11}$	N	$22.62^{+0.06}_{-0.06}$
FCC97	$17.96^{+0.09}_{-0.06}$	$14.2^{+1.2}_{-0.6}$	$25.72^{+0.08}_{-0.06}$	$0.87^{+0.00}_{-0.00}$	$1.19^{+0.15}_{-0.06}$	N	$22.75^{+0.06}_{-0.06}$
FCC100	$14.34^{+0.06}_{-0.06}$	$20.0^{+0.7}_{-0.6}$	$22.84^{+0.06}_{-0.06}$	$1.29^{+0.04}_{-0.03}$	$0.97^{+0.04}_{-0.04}$	N	$19.24^{+0.06}_{-0.06}$
FCC103	$18.40^{+0.06}_{-0.06}$	$11.7^{+0.2}_{-0.7}$	$25.75^{+0.06}_{-0.07}$	$1.15^{+0.00}_{-0.08}$	$0.94^{+0.03}_{-0.06}$	N	$22.26^{+0.06}_{-0.06}$
FCC110	$15.99^{+0.06}_{-0.06}$	$18.7^{+0.7}_{-0.6}$	$24.34^{+0.06}_{-0.06}$	$1.02^{+0.04}_{-0.03}$	$0.91^{+0.05}_{-0.04}$	N	$21.15^{+0.06}_{-0.06}$
FCC114	$18.93^{+0.21}_{-0.06}$	$9.4^{+2.0}_{-2.0}$	$25.79^{+0.20}_{-0.06}$	$1.04^{+0.14}_{-0.14}$	$1.07^{+0.21}_{-0.06}$	N	$22.61^{+0.06}_{-0.06}$
FCC116	$14.82^{+0.06}_{-0.06}$	$17.0^{+0.6}_{-0.6}$	$22.97^{+0.06}_{-0.06}$	$1.39^{+0.04}_{-0.04}$	$0.99^{+0.06}_{-0.05}$	Y	$19.60^{+0.06}_{-0.06}$
FCC123	$15.71^{+0.28}_{-0.21}$	$36.0^{+7.1}_{-4.1}$	$25.49^{+0.11}_{-0.06}$	$0.82^{+0.18}_{-0.11}$	$1.13^{+0.31}_{-0.25}$	N	$21.34^{+0.06}_{-0.06}$
FCC125	$17.93^{+0.06}_{-0.06}$	$10.1^{+0.2}_{-0.2}$	$24.95^{+0.06}_{-0.06}$	$0.70^{+0.02}_{-0.02}$	$0.77^{+0.10}_{-0.08}$	N	$22.48^{+0.06}_{-0.06}$
FCC127	$18.17^{+0.10}_{-0.24}$	$13.4^{+1.1}_{-3.0}$	$25.80^{+0.07}_{-0.30}$	$1.55^{+0.01}_{-0.30}$	$1.23^{+0.14}_{-0.25}$	N	$22.42^{+0.06}_{-0.06}$
FCC130	$17.08^{+0.11}_{-0.08}$	$21.6^{+2.0}_{-1.2}$	$25.75^{+0.08}_{-0.06}$	$0.92^{+0.11}_{-0.07}$	$1.17^{+0.30}_{-0.16}$	N	$23.23^{+0.06}_{-0.06}$
FCC131	$19.36^{+0.06}_{-0.06}$	$6.2^{+0.1}_{-0.1}$	$25.31^{+0.06}_{-0.06}$	$1.11^{+0.02}_{-0.02}$	$0.76^{+0.05}_{-0.04}$	N	$22.31^{+0.06}_{-0.06}$
FCC132	$17.40^{+0.06}_{-0.06}$	$6.6^{+0.1}_{-0.1}$	$23.49^{+0.06}_{-0.06}$	$0.91^{+0.02}_{-0.02}$	$0.81^{+0.03}_{-0.03}$	N	$20.65^{+0.06}_{-0.06}$
FCC133	$16.45^{+0.26}_{-0.15}$	$14.5^{+4.4}_{-1.8}$	$24.25^{+0.31}_{-0.14}$	$1.28^{+0.32}_{-0.20}$	$0.47^{+0.71}_{-0.40}$	Y	$20.54^{+0.06}_{-0.06}$
FCC136	$13.58^{+0.06}_{-0.06}$	$17.6^{+0.8}_{-0.5}$	$21.80^{+0.06}_{-0.06}$	$1.80^{+0.07}_{-0.04}$	$0.99^{+0.07}_{-0.06}$	Y	$17.89^{+0.06}_{-0.06}$
FCC137	$15.79^{+0.10}_{-0.08}$	$16.7^{+1.8}_{-1.2}$	$23.89^{+0.12}_{-0.09}$	$1.35^{+0.13}_{-0.10}$	$0.96^{+0.11}_{-0.09}$	Y	$20.45^{+0.06}_{-0.06}$
FCC140	$17.94^{+0.08}_{-0.07}$	$9.8^{+0.6}_{-0.4}$	$24.90^{+0.06}_{-0.06}$	$0.76^{+0.07}_{-0.05}$	$0.69^{+0.18}_{-0.15}$	Y	$21.48^{+0.06}_{-0.06}$
FCC142	$17.74^{+0.09}_{-0.07}$	$10.7^{+0.9}_{-0.6}$	$24.87^{+0.08}_{-0.06}$	$1.11^{+0.12}_{-0.09}$	$0.72^{+0.17}_{-0.14}$	Y	$21.21^{+0.06}_{-0.06}$
FCC144	$18.68^{+0.06}_{-0.06}$	$6.4^{+0.1}_{-0.1}$	$24.69^{+0.06}_{-0.06}$	$0.74^{+0.02}_{-0.02}$	$0.77^{+0.03}_{-0.03}$	N	$21.83^{+0.06}_{-0.06}$
FCC146	$18.93^{+0.06}_{-0.06}$	$5.9^{+0.0}_{-0.0}$	$24.77^{+0.06}_{-0.06}$	$0.64^{+0.01}_{-0.01}$	$0.61^{+0.05}_{-0.04}$	Y	$21.72^{+0.06}_{-0.06}$
FCC156	$16.37^{+0.06}_{-0.06}$	$14.6^{+0.3}_{-0.3}$	$24.19^{+0.06}_{-0.06}$	$0.93^{+0.02}_{-0.02}$	$0.70^{+0.03}_{-0.03}$	N	$21.24^{+0.06}_{-0.06}$
FCC157	$17.22^{+0.33}_{-0.10}$	$15.8^{+6.5}_{-1.3}$	$25.21^{+0.42}_{-0.08}$	$1.04^{+0.47}_{-0.13}$	$0.90^{+0.34}_{-0.13}$	Y	$21.87^{+0.06}_{-0.06}$
FCC158	$15.76^{+0.17}_{-0.10}$	$22.4^{+3.9}_{-1.9}$	$24.51^{+0.18}_{-0.09}$	$1.09^{+0.21}_{-0.11}$	$0.90^{+0.29}_{-0.15}$	Y	$20.21^{+0.06}_{-0.06}$
FCC160	$16.60^{+0.09}_{-0.07}$	$13.6^{+1.2}_{-0.8}$	$24.25^{+0.08}_{-0.06}$	$1.03^{+0.11}_{-0.07}$	$0.78^{+0.28}_{-0.09}$	Y	$21.07^{+0.06}_{-0.06}$
FCC165	$16.65^{+0.06}_{-0.06}$	$14.3^{+0.3}_{-0.3}$	$24.42^{+0.06}_{-0.06}$	$0.77^{+0.02}_{-0.02}$	$0.82^{+0.04}_{-0.04}$	Y	$21.14^{+0.06}_{-0.06}$

Notes. Column keys: (1) Galaxy name from the Fornax Cluster Catalog (Ferguson, 1989). (2) i-band magnitude as determined by Galfit (in magnitudes). (3) Effective radius in arcsec from Galfit-fitting. (4) Calculated effective mean surface brightness (in magnitudes per square arcsec). (5) Sérsic index. (6) Galaxy (g'-i') colour (in magnitudes). (7) Nucleated fit (Y) or non-nucleated fit (N). (8) i'-band central magnitude.

Table A.3: *Results for sample galaxies in the u'-band and galactic (u'-g') colour.*

Name	u' (mag)	$r_{e,u}$ (")	$\langle\mu\rangle_e$ (mag/"^{2})	n_u	(u'-g') (mag)	nucl.	u'$_n$ (mag)
(1)	(2)	(3)	(4)	(5)	(6)	(7)	(8)
FCC85	$17.55^{+0.08}_{-0.08}$	$15.3^{+0.3}_{-0.3}$	$25.46^{+0.08}_{-0.08}$	$1.26^{+0.03}_{-0.03}$	$1.62^{+0.04}_{-0.03}$	Y	$22.05^{+0.08}_{-0.08}$
FCC86	$18.50^{+0.08}_{-0.08}$	$18.8^{+0.5}_{-0.5}$	$26.87^{+0.08}_{-0.08}$	$1.08^{+0.03}_{-0.03}$	$1.31^{+0.10}_{-0.08}$	N	$23.68^{+0.08}_{-0.08}$
FCC93	$21.72^{+0.12}_{-0.11}$	$5.6^{+0.4}_{-0.3}$	$27.45^{+0.08}_{-0.08}$	$0.45^{+0.05}_{-0.05}$	$2.14^{+0.19}_{-0.17}$	N	$25.53^{+0.08}_{-0.08}$
FCC94	$20.42^{+0.08}_{-0.08}$	$9.7^{+0.4}_{-0.3}$	$27.36^{+0.08}_{-0.08}$	$0.83^{+0.05}_{-0.04}$	$0.95^{+0.12}_{-0.10}$	N	$24.99^{+0.08}_{-0.08}$
FCC97	$20.39^{+0.08}_{-0.48}$	$27.6^{+15.2}_{-15.2}$	$29.59^{+0.08}_{-1.25}$	$1.46^{+0.03}_{-0.03}$	$1.24^{+0.13}_{-0.48}$	N	$24.89^{+0.08}_{-0.08}$
FCC100	$16.85^{+0.08}_{-0.08}$	$17.6^{+0.4}_{-0.4}$	$25.07^{+0.08}_{-0.08}$	$1.04^{+0.03}_{-0.03}$	$1.54^{+0.04}_{-0.04}$	Y	$21.85^{+0.08}_{-0.08}$
FCC103	$20.04^{+0.08}_{-0.08}$	$13.1^{+0.5}_{-0.4}$	$27.62^{+0.08}_{-0.08}$	$0.83^{+0.02}_{-0.02}$	$0.70^{+0.06}_{-0.05}$	N	$24.35^{+0.08}_{-0.08}$
FCC110	$18.41^{+0.08}_{-0.08}$	$17.0^{+0.8}_{-0.7}$	$26.56^{+0.08}_{-0.08}$	$0.79^{+0.05}_{-0.04}$	$1.51^{+0.07}_{-0.07}$	N	$24.17^{+0.08}_{-0.08}$
FCC114	$21.08^{+0.13}_{-0.11}$	$9.5^{+0.8}_{-0.6}$	$27.97^{+0.08}_{-0.08}$	$1.00^{+0.00}_{-0.00}$	$1.07^{+0.14}_{-0.11}$	N	$24.70^{+0.08}_{-0.08}$
FCC116	$17.40^{+0.08}_{-0.08}$	$15.5^{+0.4}_{-0.3}$	$25.34^{+0.08}_{-0.08}$	$1.34^{+0.02}_{-0.02}$	$1.58^{+0.05}_{-0.04}$	N	$22.39^{+0.08}_{-0.08}$
FCC123	$18.26^{+0.15}_{-0.14}$	$31.1^{+2.3}_{-1.9}$	$27.72^{+0.08}_{-0.08}$	$0.56^{+0.05}_{-0.04}$	$1.41^{+0.21}_{-0.19}$	N	$23.80^{+0.08}_{-0.08}$
FCC125	$20.37^{+0.08}_{-0.08}$	$8.4^{+0.4}_{-0.0}$	$26.97^{+0.08}_{-0.08}$	$0.71^{+0.02}_{-0.07}$	$1.66^{+0.10}_{-0.10}$	N	$24.80^{+0.08}_{-0.08}$
FCC127	$20.62^{+0.08}_{-0.08}$	$9.8^{+0.4}_{-0.3}$	$27.57^{+0.08}_{-0.08}$	$1.00^{+0.00}_{-0.00}$	$1.22^{+0.10}_{-0.08}$	N	$25.05^{+0.08}_{-0.08}$
FCC130	$20.16^{+0.08}_{-0.08}$	$18.8^{+0.3}_{-0.3}$	$28.53^{+0.08}_{-0.08}$	$0.20^{+0.00}_{-0.01}$	$1.91^{+0.28}_{-0.15}$	N	$24.77^{+0.08}_{-0.08}$
FCC131	$21.37^{+0.36}_{-0.20}$	$7.0^{+2.4}_{-0.9}$	$27.59^{+0.29}_{-0.09}$	$0.90^{+0.05}_{-0.04}$	$1.26^{+0.36}_{-0.21}$	N	$24.70^{+0.08}_{-0.08}$
FCC132	$19.61^{+0.08}_{-0.08}$	$7.0^{+0.3}_{-0.2}$	$25.84^{+0.08}_{-0.08}$	$0.91^{+0.04}_{-0.03}$	$1.40^{+0.05}_{-0.04}$	N	$23.34^{+0.08}_{-0.08}$
FCC133	$19.01^{+0.26}_{-0.12}$	$13.7^{+3.7}_{-1.1}$	$26.69^{+0.25}_{-0.08}$	$0.90^{+0.36}_{-0.11}$	$2.09^{+0.71}_{-0.38}$	Y	$23.10^{+0.08}_{-0.08}$
FCC136	$16.17^{+0.12}_{-0.10}$	$17.4^{+2.3}_{-1.5}$	$24.38^{+0.14}_{-0.10}$	$1.59^{+0.19}_{-0.14}$	$1.61^{+0.14}_{-0.11}$	Y	$20.92^{+0.08}_{-0.08}$
FCC137	$18.12^{+0.16}_{-0.13}$	$17.5^{+3.1}_{-2.0}$	$26.33^{+0.20}_{-0.14}$	$1.42^{+0.19}_{-0.15}$	$1.38^{+0.17}_{-0.14}$	Y	$23.05^{+0.08}_{-0.08}$
FCC140	$20.14^{+0.13}_{-0.08}$	$10.4^{+1.4}_{-0.5}$	$27.23^{+0.14}_{-0.08}$	$0.86^{+0.21}_{-0.08}$	$1.50^{+0.21}_{-0.15}$	Y	$23.84^{+0.08}_{-0.08}$
FCC142	$19.64^{+0.14}_{-0.11}$	$16.2^{+1.5}_{-1.0}$	$27.68^{+0.08}_{-0.08}$	$1.15^{+0.13}_{-0.06}$	$1.18^{+0.20}_{-0.16}$	Y	$23.79^{+0.08}_{-0.08}$
FCC144	$20.84^{+0.08}_{-0.08}$	$6.4^{+0.5}_{-0.3}$	$26.87^{+0.09}_{-0.08}$	$0.86^{+0.09}_{-0.07}$	$1.39^{+0.09}_{-0.07}$	N	$24.23^{+0.08}_{-0.08}$
FCC146	$20.94^{+0.08}_{-0.08}$	$6.7^{+0.3}_{-0.2}$	$27.06^{+0.08}_{-0.08}$	$0.86^{+0.04}_{-0.03}$	$1.40^{+0.07}_{-0.06}$	N	$24.34^{+0.08}_{-0.08}$
FCC156	$18.44^{+0.08}_{-0.08}$	$15.7^{+0.5}_{-0.5}$	$26.42^{+0.08}_{-0.08}$	$0.91^{+0.03}_{-0.03}$	$1.37^{+0.05}_{-0.04}$	N	$23.84^{+0.08}_{-0.08}$
FCC157	$19.84^{+0.08}_{-0.08}$	$12.1^{+0.0}_{-0.0}$	$27.25^{+0.08}_{-0.08}$	$0.85^{+0.00}_{-0.00}$	$1.71^{+0.10}_{-0.11}$	N	$24.69^{+0.08}_{-0.08}$
FCC158	$18.62^{+0.08}_{-0.08}$	$15.6^{+0.3}_{-0.3}$	$26.58^{+0.08}_{-0.08}$	$0.78^{+0.02}_{-0.02}$	$1.96^{+0.24}_{-0.12}$	Y	$22.78^{+0.08}_{-0.08}$
FCC160	$19.09^{+0.08}_{-0.08}$	$14.0^{+0.7}_{-0.6}$	$26.81^{+0.08}_{-0.08}$	$1.19^{+0.06}_{-0.04}$	$1.71^{+0.27}_{-0.07}$	N	$23.71^{+0.08}_{-0.08}$
FCC165	$18.77^{+0.08}_{-0.08}$	$16.8^{+0.7}_{-0.6}$	$26.89^{+0.08}_{-0.08}$	$0.93^{+0.05}_{-0.04}$	$1.30^{+0.06}_{-0.05}$	N	$23.76^{+0.08}_{-0.08}$

Notes. Column keys: (1) Galaxy name from the Fornax Cluster Catalog (Ferguson, 1989). (2) u-band magnitude as determined by Galfit (in magnitudes). (3) Effective radius in arcsec from Galfit-fitting. (4) Calculated effective mean surface brightness (in magnitudes per square arcsec). (5) Sérsic index. (6) Galaxy (u'-g') colour (in magnitudes). (7) Nucleated fit (Y) or non-nucleated fit (N). (8) u'-band central magnitude. No convolution was used for the central parameters in this band, so they cannot be well compared to those of other bands.

Bibliography

M. Arnaboldi, M. Capaccioli, D. Mancini, P. Rafanelli, R. Scaramella, G. Sedmak, and G. P. Vettolani. VST: VLT Survey Telescope. *The Messenger*, 93:30–35, September 1998.

K. Bekki, W. J. Couch, and M. J. Drinkwater. Galaxy Threshing and the Formation of Ultracompact Dwarf Galaxies. ApJ, 552:L105–L108, May 2001. doi: 10.1086/320339.

R. Bender, D. Burstein, and S. M. Faber. Dynamically hot galaxies. I - Structural properties. ApJ, 399:462–477, November 1992. doi: 10.1086/171940.

E. Bertin and S. Arnouts. SExtractor: Software for source extraction. A&AS, 117:393–404, June 1996. doi: 10.1051/aas:1996164.

B. Binggeli and L. M. Cameron. Dwarf galaxies in the Virgo cluster. I - The systematic photometric properties of early-type dwarfs. A&A, 252:27–52, December 1991.

J. P. Blakeslee, A. Jordán, S. Mei, P. Côté, L. Ferrarese, L. Infante, E. W. Peng, J. L. Tonry, and M. J. West. The ACS Fornax Cluster Survey. V. Measurement and Recalibration of Surface Brightness Fluctuations and a Precise Value of the Fornax-Virgo Relative Distance. ApJ, 694: 556–572, March 2009. doi: 10.1088/0004-637X/694/1/556.

F. Bonnarel, P. Fernique, O. Bienaymé, D. Egret, F. Genova, M. Louys, F. Ochsenbein, M. Wenger, and J. G. Bartlett. The ALADIN interactive sky atlas. A reference tool for identification of astronomical sources. A&AS, 143:33–40, April 2000. doi: 10.1051/aas:2000331.

N. Caon, M. Capaccioli, and M. D'Onofrio. On the Shape of the Light Profiles of Early Type Galaxies. MNRAS, 265:1013, December 1993. doi: 10.1093/mnras/265.4.1013.

M. J. Currie, D. S. Berry, T. Jenness, A. G. Gibb, G. S. Bell, and P. W. Draper. Starlink Software in 2013. In N. Manset and P. Forshay, editors, *Astronomical Data Analysis Software and Systems XXIII*, volume 485 of *Astronomical Society of the Pacific Conference Series*, page 391, May 2014.

J. T. A. de Jong, G. A. Verdoes Kleijn, D. R. Boxhoorn, H. Buddelmeijer, M. Capaccioli, F. Getman, A. Grado, E. Helmich, Z. Huang, N. Irisarri, K. Kuijken, F. La Barbera, J. P. McFarland, N. R. Napolitano, M. Radovich, G. Sikkema, E. A. Valentijn, K. G. Begeman, M. Brescia, S. Cavuoti, A. Choi, O.-M. Cordes, G. Covone, M. Dall'Ora, H. Hildebrandt, G. Longo, R. Nakajima, M. Paolillo, E. Puddu, A. Rifatto, C. Tortora, E. van Uitert, A. Buddendiek, J. Harnois-Déraps, T. Erben, M. B. Eriksen, C. Heymans, H. Hoekstra, B. Joachimi, T. D. Kitching, D. Klaes, L. V. E. Koopmans, F. Köhlinger, N. Roy, C. Sifón, P. Schneider, W. J. Sutherland, M. Viola, and W.-J. Vriend. The first and second data releases of the Kilo-Degree Survey. A&A, 582:A62, October 2015. doi: 10.1051/0004-6361/201526601.

S. De Rijcke, P. Buyle, and M. Koleva. FCC046: A Candidate Gaseous Polar Ring Dwarf Elliptical Galaxy in the Fornax Cluster. ApJ, 770:L26, June 2013. doi: 10.1088/2041-8205/770/2/L26.

M. den Brok, R. F. Peletier, E. A. Valentijn, M. Balcells, D. Carter, P. Erwin, H. C. Ferguson, P. Goudfrooij, A. W. Graham, D. Hammer, J. R. Lucey, N. Trentham, R. Guzmán, C. Hoyos, G. Verdoes Kleijn, S. Jogee, A. M. Karick, I. Marinova, M. Mouhcine, and T. Weinzirl. The HST/ACS Coma Cluster Survey - VI. Colour gradients in giant and dwarf early-type galaxies. MNRAS, 414:3052–3070, July 2011. doi: 10.1111/j.1365-2966.2011.18606.x.

M. den Brok, R. F. Peletier, A. Seth, M. Balcells, L. Dominguez, A. W. Graham, D. Carter, P. Erwin, H. C. Ferguson, P. Goudfrooij, R. Guzmán, C. Hoyos, S. Jogee, J. Lucey, S. Phillipps, T. Puzia, E. Valentijn, G. V. Kleijn, and T. Weinzirl. The HST/ACS Coma Cluster Survey - X. Nuclear star clusters in low-mass early-type galaxies: scaling relations. MNRAS, 445:2385–2403, December 2014. doi: 10.1093/mnras/stu1906.

M. J. Drinkwater, M. D. Gregg, and M. Colless. Substructure and Dynamics of the Fornax Cluster. ApJ, 548:L139–L142, February 2001. doi: 10.1086/319113.

H. C. Ferguson. Population studies in groups and clusters of galaxies. II - A catalog of galaxies in the central 3.5 deg of the Fornax Cluster. AJ, 98:367–418, August 1989. doi: 10.1086/115152.

L. Ferrarese, P. Côté, A. Jordán, E. W. Peng, J. P. Blakeslee, S. Piatek, S. Mei, D. Merritt, M. Milosavljević, J. L. Tonry, and M. J. West. The ACS Virgo Cluster Survey. VI. Isophotal Analysis and the Structure of Early-Type Galaxies. ApJS, 164:334–434, June 2006. doi: 10.1086/501350.

M. Fukugita, K. Shimasaku, and T. Ichikawa. Galaxy Colors in Various Photometric Band Systems. PASP, 107:945, October 1995. doi: 10.1086/133643.

L. Glass, L. Ferrarese, P. Côté, A. Jordán, E. Peng, J. P. Blakeslee, C.-W. Chen, L. Infante, S. Mei, J. L. Tonry, and M. J. West. The ACS Fornax Cluster Survey. IV. Deprojection of the Surface Brightness Profiles of Early-type Galaxies in the Virgo and Fornax Clusters: Investigating the "Core/Power-law Dichotomy". ApJ, 726:31, January 2011. doi: 10.1088/0004-637X/726/1/31.

A. W. Graham and S. P. Driver. A Concise Reference to (Projected) Sérsic $R^{1/n}$ Quantities, Including Concentration, Profile Slopes, Petrosian Indices, and Kron Magnitudes. *Publications of the Astronomical Society in Australia*, 22:118–127, 2005. doi: 10.1071/AS05001.

A. W. Graham and R. Guzmán. HST Photometry of Dwarf Elliptical Galaxies in Coma, and an Explanation for the Alleged Structural Dichotomy between Dwarf and Bright Elliptical Galaxies. AJ, 125:2936–2950, June 2003. doi: 10.1086/374992.

E. Hamraz, R. Peletier, H. Khosroshahi, and E. Valentijn. Young stellar populations in early-type dwarf galaxies in nearby galaxy clusters. In preparation, 2017.

C. Hoyos, M. den Brok, G. Verdoes Kleijn, D. Carter, M. Balcells, R. Guzmán, R. Peletier, H. C. Ferguson, P. Goudfrooij, A. W. Graham, D. Hammer, A. M. Karick, J. R. Lucey, A. Matković, D. Merritt, M. Mouhcine, and E. Valentijn. The HST/ACS Coma Cluster Survey - III. Structural parameters of galaxies using single Sérsic fits. MNRAS, 411:2439–2460, March 2011. doi: 10.1111/j.1365-2966.2010.17855.x.

J. Janz and T. Lisker. The Sizes of Early-Type Galaxies. ApJ, 689:L25, December 2008. doi: 10.1086/595720.

J. Janz and T. Lisker. On the Color-Magnitude Relation of Early-Type Galaxies. ApJ, 696: L102–L105, May 2009. doi: 10.1088/0004-637X/696/1/L102.

G. Kauffmann and M. Haehnelt. A unified model for the evolution of galaxies and quasars. MNRAS, 311:576–588, January 2000. doi: 10.1046/j.1365-8711.2000.03077.x.

S. Kim, S.-C. Rey, T. Lisker, and S. T. Sohn. Color-Magnitude Relations of Early-type Dwarf Galaxies in the Virgo Cluster: An Ultraviolet Perspective. ApJ, 721:L72–L77, September 2010. doi: 10.1088/2041-8205/721/1/L72.

M. Koleva, S. de Rijcke, P. Prugniel, W. W. Zeilinger, and D. Michielsen. Formation and evolution of dwarf elliptical galaxies - II. Spatially resolved star formation histories. MNRAS, 396:2133–2151, July 2009. doi: 10.1111/j.1365-2966.2009.14820.x.

J. Kormendy. Brightness distributions in compact and normal galaxies. II - Structure parameters of the spheroidal component. ApJ, 218:333–346, December 1977. doi: 10.1086/155687.

J. Kormendy, D. B. Fisher, M. E. Cornell, and R. Bender. Structure and Formation of Elliptical and Spheroidal Galaxies. ApJS, 182:216–309, May 2009. doi: 10.1088/0067-0049/182/1/216.

K. Kuijken. OmegaCAM: ESO's Newest Imager. *The Messenger*, 146:8–11, December 2011.

K. Kuijken, R. Bender, E. Cappellaro, B. Muschielok, A. Baruffolo, E. Cascone, O. Iwert, W. Mitsch, H. Nicklas, E. A. Valentijn, D. Baade, K. G. Begeman, A. Bortolussi, D. Boxhoorn, F. Christen, E. R. Deul, C. Geimer, L. Greggio, R. Harke, R. Häfner, G. Hess, H.-J. Hess, U. Hopp, I. Ilijevski, G. Klink, H. Kravcar, J. L. Lizon, C. E. Magagna, P. Müller, R. Niemeczek, L. de Pizzol, H. Poschmann, K. Reif, R. Rengelink, J. Reyes, A. Silber, and W. Wellem. OmegaCAM: the 16k×16k CCD camera for the VLT survey telescope. *The Messenger*, 110:15–18, December 2002.

T. Lisker, K. Glatt, P. Westera, and E. K. Grebel. Virgo Cluster Early-Type Dwarf Galaxies with the Sloan Digital Sky Survey. II. Early-Type Dwarfs with Central Star Formation. AJ, 132:2432–2452, December 2006. doi: 10.1086/508414.

J. M. Lotz, B. W. Miller, and H. C. Ferguson. The Colors of Dwarf Elliptical Galaxy Globular Cluster Systems, Nuclei, and Stellar Halos. ApJ, 613:262–278, September 2004. doi: 10.1086/422871.

S. Mahajan, M. J. Drinkwater, S. Driver, L. S. Kelvin, A. M. Hopkins, I. Baldry, S. Phillipps, J. Bland-Hawthorn, S. Brough, J. Loveday, S. J. Penny, and A. S. G. Robotham. Galaxy And Mass Assembly (GAMA): the unimodal nature of the dwarf galaxy population. MNRAS, 446:2967–2984, January 2015. doi: 10.1093/mnras/stu2009.

J. P. McFarland, G. Verdoes-Kleijn, G. Sikkema, E. M. Helmich, D. R. Boxhoorn, and E. A. Valentijn. The Astro-WISE optical image pipeline. Development and implementation. *Experimental Astronomy*, 35:45–78, January 2013. doi: 10.1007/s10686-011-9266-x.

D. Michielsen, A. Boselli, C. J. Conselice, E. Toloba, I. M. Whiley, A. Aragón-Salamanca, M. Balcells, N. Cardiel, A. J. Cenarro, J. Gorgas, R. F. Peletier, and A. Vazdekis. The relation between stellar populations, structure and environment for dwarf elliptical galaxies from the MAGPOP-ITP. MNRAS, 385:1374–1392, April 2008. doi: 10.1111/j.1365-2966.2008.12846.x.

S. Mieske, M. Hilker, L. Infante, and C. Mendes de Oliveira. The early-type dwarf galaxy population of the Fornax cluster. A&A, 463:503–512, February 2007. doi: 10.1051/0004-6361:20066300.

I. Misgeld, S. Mieske, and M. Hilker. The early-type dwarf galaxy population of the Hydra I cluster. A&A, 486:697–709, August 2008. doi: 10.1051/0004-6361:200810014.

I. Misgeld, M. Hilker, and S. Mieske. The early-type dwarf galaxy population of the Centaurus cluster. A&A, 496:683–693, March 2009. doi: 10.1051/0004-6361/200811451.

B. Moore, S. Ghigna, F. Governato, G. Lake, T. Quinn, J. Stadel, and P. Tozzi. Dark Matter Substructure within Galactic Halos. ApJ, 524:L19–L22, October 1999. doi: 10.1086/312287.

R. P. Muñoz, P. Eigenthaler, T. H. Puzia, M. A. Taylor, Y. Ordenes-Briceño, K. Alamo-Martínez, K. X. Ribbeck, S. Ángel, M. Capaccioli, P. Côté, L. Ferrarese, G. Galaz, M. Hempel, M. Hilker, A. Jordán, A. Lançon, S. Mieske, M. Paolillo, T. Richtler, R. Sánchez-Janssen, and H. Zhang. Unveiling a Rich System of Faint Dwarf Galaxies in the Next Generation Fornax Survey. ApJ, 813:L15, November 2015. doi: 10.1088/2041-8205/813/1/L15.

M. Pak, S.-C. Rey, T. Lisker, Y. Lee, S. Kim, E.-C. Sung, H. Jerjen, and J. Chung. The properties of early-type galaxies in the Ursa Major cluster. MNRAS, 445:630–647, November 2014. doi: 10.1093/mnras/stu1722.

C. Y. Peng, L. C. Ho, C. D. Impey, and H.-W. Rix. Detailed Decomposition of Galaxy Images. II. Beyond Axisymmetric Models. AJ, 139:2097–2129, June 2010. doi: 10.1088/0004-6256/139/6/2097.

R. Sánchez-Janssen, L. Ferrarese, L. A. MacArthur, P. Côté, J. P. Blakeslee, J.-C. Cuillandre, P.-A. Duc, P. Durrell, S. Gwyn, A. W. McConnacchie, A. Boselli, S. Courteau, E. Emsellem, S. Mei, E. Peng, T. H. Puzia, J. Roediger, L. Simard, F. Boyer, and M. Santos. The Next Generation Virgo Cluster Survey. VII. The Intrinsic Shapes of Low-luminosity Galaxies in the Core of the Virgo Cluster, and a Comparison with the Local Group. ApJ, 820:69, March 2016. doi: 10.3847/0004-637X/820/1/69.

P. Schipani, M. Capaccioli, C. Arcidiacono, J. Argomedo, M. Dall'Ora, S. D'Orsi, J. Farinato, D. Magrin, L. Marty, R. Ragazzoni, and G. Umbriaco. VST: from commissioning to science. In *Ground-based and Airborne Telescopes IV*, volume 8444 of Proc. SPIE, page 84441C, September 2012. doi: 10.1117/12.925481.

J. L. Sérsic. *Atlas de galaxias australes*. 1968.

V. Springel, J. Wang, M. Vogelsberger, A. Ludlow, A. Jenkins, A. Helmi, J. F. Navarro, C. S. Frenk, and S. D. M. White. The Aquarius Project: the subhaloes of galactic haloes. MNRAS, 391:1685–1711, December 2008. doi: 10.1111/j.1365-2966.2008.14066.x.

M. L. Turner, P. Côté, L. Ferrarese, A. Jordán, J. P. Blakeslee, S. Mei, E. W. Peng, and M. J. West. The ACS Fornax Cluster Survey. VI. The Nuclei of Early-type Galaxies in the Fornax Cluster. ApJS, 203:5, November 2012. doi: 10.1088/0067-0049/203/1/5.

A. Venhola, R. Peletier, H. Salo, E. Laurikainen, T. Lisker, M. Capaccioli, G. Verdoes Kleijn, and FDS collaboration. The Fornax Deep Survey (FDS) with VST: II. Low surface brightness galaxies in the Fornax cluster center. In preparation, 2017.